Improving Fringe Projection Profilometry for in-situ Monitoring of Laser Powder Bed Fusion Processes

by

Sizhe Xu

Bachelor of Engineering, Wuhan University of Technology, 2020

Submitted to the Graduate Faculty of the

Swanson School of Engineering in partial fulfillment

of the requirements for the degree of

Master of Science

University of Pittsburgh

2023

UNIVERSITY OF PITTSBURGH

SWANSON SCHOOL OF ENGINEERING

This thesis was presented

by

Sizhe Xu

It was defended on

February 23, 2023

and approved by

Xiayun Zhao, Ph.D., Assistant Professor, Department of Mechanical Engineering and Materials Science

Albert To, Ph.D., Professor and William Kepler Whiteford Professor, Department of Mechanical Engineering and Materials Science

William Clark, Ph.D., Professor, Department of Mechanical Engineering and Materials Science

Thesis Advisor: Xiayun Zhao, PhD, Assistant Professor, Department of Mechanical Engineering and Materials Science

Improving Fringe Projection Profilometry for in-situ Monitoring of Laser Powder Bed Fusion Processes

Sizhe Xu, MS

University of Pittsburgh, 2023

3D shape measurements are critical in a range of industries, ranging from manufacturing to art conservation. Many existing techniques are contact methods, which are time-consuming and material-contaminating. While non-contact technologies have their benefits, many current systems are limited in their functionality. The goal of this project is to improve a fringe projection-based system for 3D shape measurements, especially in laser powder bed fusion process (L-PBF) based metal AM.

Fringe projection profilometry (FPP) is a low-cost, high-precision, and high-resolution optics-based 3D measurement technology. Several researchers have demonstrated that FPP can swiftly evaluate surface topography without contacting or interrupting the process during L-PBF. However, due to the complex physics and heterogeneous materials in L-PBF processes, the FPP method, which is based on dynamic light intensity, may result in inaccurate 3D reconstruction of printed layers and objects. Associated with the metal surface's high specular reflectivity, a glossy saturated portion is likely to present in a FPP camera image and conceal the fringe pattern, causing the height information linked with it to be lost. In this work, we propose two methods to improve FPP for in-situ monitoring of surface topography during L-PBF processes. The first method is to use a 12-step phase-shifted FPP approach instead of the conventional 3-step phase-shifted FPP method. The second method is to place an orthogonal linear polarizer in front of the camera and the projector lens, respectively, in an attempt to lessen the effect of specular reflection from the

metal surface. The surface heights of printed sample blocks are measured using the proposed in-situ FPP methods as well as an ex-situ Keyence microscope. By comparing the FPP and Keyence measurement results, we can determine the influence of increasing projected fringe phase steps and that of employing linear polarizers. The experimental results show that the proposed methods can help reduce the overexposed area ratio from 24.52% to 0.28% in specific experiment setup. And the polarized FPP method could reduce the root-mean-square error from 15.75 to 10.97 in 3-step phase shifting, and also reduced the RMSE from 15.75 to 12.51 between 3-step non-polarized and 12-step with polarizers.

Table of Content

List of Tables

List of Figures

Acknowledgements

There are many key points in life, and there are also many people and many thanks to be remembered in life.

This paper was completed under the careful guidance and instruction of my supervisor, Dr. Xiayun Zhao, whose efforts and sweat have helped me to grasp the direction of my thesis and complete it successfully. I would like to express my most sincere gratitude to my supervisors for their wise teachings and kind care, which are still vivid in my mind.

I would also like to thank my committee members, Dr. Albert To and Dr. William Clark, for taking time out of their busy schedules to guide me and give me critical comments on my dissertation.

I am also grateful to Haolin Zhang, my lab-mate, who has been selflessly helping me, guiding and helping me in my professional and scientific work. I am very grateful to have met such a wonderful teacher and friend.

Last but not least, I would like to thank my parents. They are the strong support for me on my way to school, and they help me to solve my problems when I face the confusion of life choices.

1.0 Introduction

In the late 1980s, the United States was the birthplace of additive manufacturing (AM) technology. AM, often known as "rapid prototyping" technology, was created out of a necessity for quick model creation in the beginning. AM is the polar opposite of traditional material "removal" processing methods, which are based on 3D CAD model data and add material, usually using layer-by-layer manufacturing methods, to directly create 3D physical solid models that are identical to corresponding mathematical models. After forty years of rapid technological advancement, AM has progressed from conceptual model rapid prototyping to an advanced manufacturing technology that encompasses all aspects of product design, research and development, and manufacturing, far surpassing the original rapid prototyping technology.

New concepts for the quick fabrication of complicated items are made possible by the advent of AM technology. For instance, the building of conformal cooling channels was previously restricted by the linear restrictions of drilling operations [Sachs, E., Wylonis, E., Allen, S., Cima, & Guo, H. 2000]. Therefore, tool access requirements have been a challenge when producing tools for injection molding applications. On the other hand, compared to methods like injection molding, AM can support short production runs without obstructing the needs of most processing technologies for tool access [Ian Gibson I G. 2015].The LPBF (Laser Powder Bed Fusion) process in AM technology overall, as well as the material characteristics of the final component, can be significantly impacted by changes in process parameters or circumstances, such as laser parameters, build environment process gases, moisture, and conditions of metal powders [Mani M, Feng S, Lane B, et al. 2015]. However, other issues also occur. How to quantify the surface morphology

becomes crucial since the mechanical characteristics of layer stacked systems are frequently intricately tied to the surface morphology.

1.1 Laser Powder Bed Fusion

Metal AM technology, which is even referred to as the "driver of the third industrial revolution," brings new perspectives and insights to the manufacturing business by adding materials to the print bed in a precise method layer by layer [Gu, Dongdong. 2015]. When opposed to traditional manufacturing technologies' intricate process planning, metal AM is a new technique that makes the process of creating 3D objects simpler. Laser powder bed fusion (LPBF) is a cutting-edge metal AM technique. It presently provides the highest repeatability and density for component manufacture, and as a result, it is extensively researched in both industry and academia.

In general, the LPBF process fabricates components using the following steps:

(1) Lower the build platform to the layer thickness specified in the design.

(2) Spread the new powder layer by repositioning the recoater across the powder bed and/or part surface to achieve a consistent powder layer thickness equal to the actual layer thickness.

(3) Start the laser and scan the powder layer's exterior and interior contours using the laser settings specified in the LPBF design file to finish a single layer of printing.

The specific system structure, as shown in Fig. 1. To conclude, the LPBF process involves layer-by-layer powder recoating, laser scanning, and melting until the final product is completed. The entire procedure is carried out in a sealed chamber with an inert atmosphere to prevent interference from outside influences.

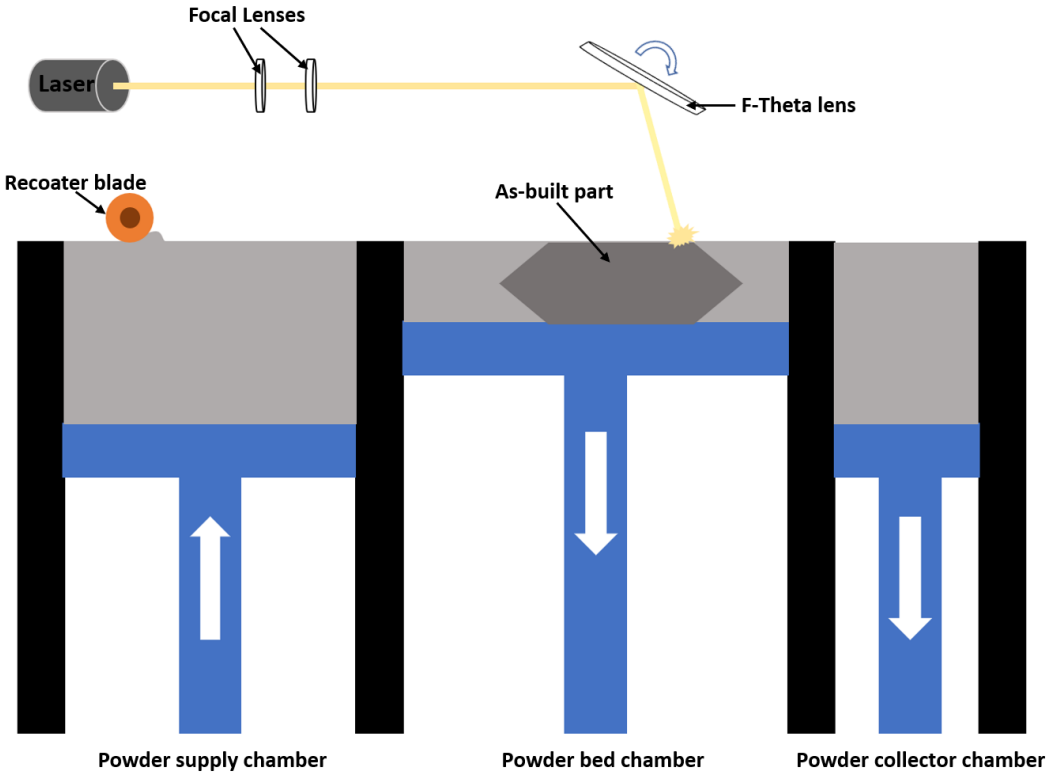

Fig. 1. Schematic illustration of the laser-based powder bed fusion process [Antonella Sola, Alireza Nouri, 2019].

A range of process factors, including but not limited to beam power, scan speed, hatch spacing, layer thickness, and scan pattern, govern the favorable process results of LPBF metal AM constructions. The geometry, local organization, defect size, and defect morphology of the melt pool are substantially determined by the combination of these process factors. Importantly, undesirable LPBF defects such as porosity, inclusions, and oxides are harmful to the structural integrity and longevity of metal AM components, especially in aerospace and biomedical applications where the defect structure is predominantly responsible for early failure (e.g., fatigue).

1.2 Surface Topography in LPBF

Metal AM provides advantages in terms of speeding up the production of complicated geometric items, but it also has drawbacks. In recent years, further study has discovered that LPBF can build complex structures under more suitable process conditions than classic methods like milling and cutting, and how to industrialize LPBF has been a hot topic of research. Mechanical properties are frequently intricately connected to product surface topography. Surface texture has gained significant attention in recent years across a wide range of industries. When deciding whether a part is adequate or not, surface roughness in particular is crucial. Surface finish is helpful in machine tool monitoring, which is also utilized in engineering applications. Here is a discussion of these characteristics. However, it is vital to take into account how the significance of surface roughness evolves over time and how it is influenced by the workpiece's real size and the production process. Smaller objects undergo modifications that highlight the significance of the surface [Whitehouse, David J. 1997].

Metal AM products' mechanical properties have been noted to be inconsistent. The major cause for this is porosity defects such as lack-of-fusion porosity, keyhole porosity, balling, and gas porosity that arise during the manufacturing process, as shown in Fig. 2. The causes of these topography defects are linked to several process variables. The key to analyzing the intuitive mechanical and physical properties of metal AM products is to get reliable surface topography.

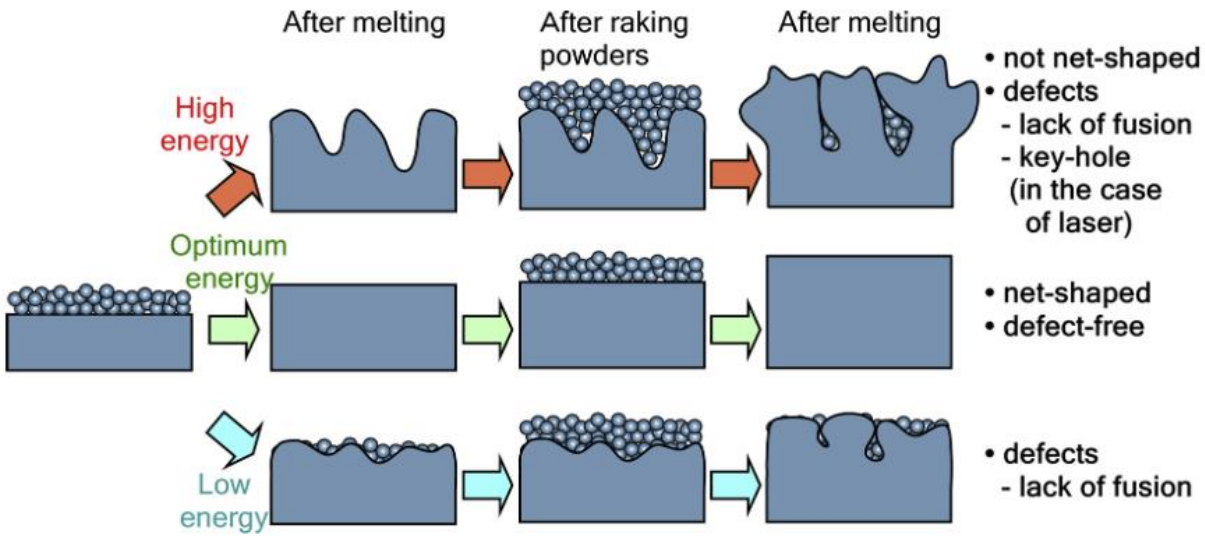

Fig. 2. Diagram of the relationships between layer surface topography and defect formation in a laser powder bed fusion addtive manufacturing process[K Aoyagi, H Wang, H Sudo, A Chiba, 2019].

As stated previously, LPBF use a laser source to melt powder material, which is then constructed layer by layer to create a three-dimensional component in a region. The laser may produce welding tracks on a given thickness layer of metal powder by modifying process parameters such as power (P), scanning speed (V), and hatching spacing (H). To generate the volume and surface necessary for the 3D part, these trajectories are cooled and solidified. This method of object creation results in the construction of two distinct surfaces: i) the top surface, which is made by the last layer's laser tracks; ii) the sides, which are formed by the starting and end tracks of all layers, as show in Fig. 3. Compared to the roughness of the conventional manufacturing process, the average values of the surface roughness of LPBF obtained so far by a large number of experiments (top surface R_a: 8-20 μm and sides R_a: 15-35 μm) [Calignano F, Manfredi D, Ambrosio E P, et al., 2013]. According with study findings, achieving the minimal R_a on both the top and side surfaces at the same time is challenging. The formation of top and side

surfaces is, in essence, the result of separate mechanisms. [Stimpson, C. K., Snyder, J. C., Thole, K. A., and colleagues, 2016].

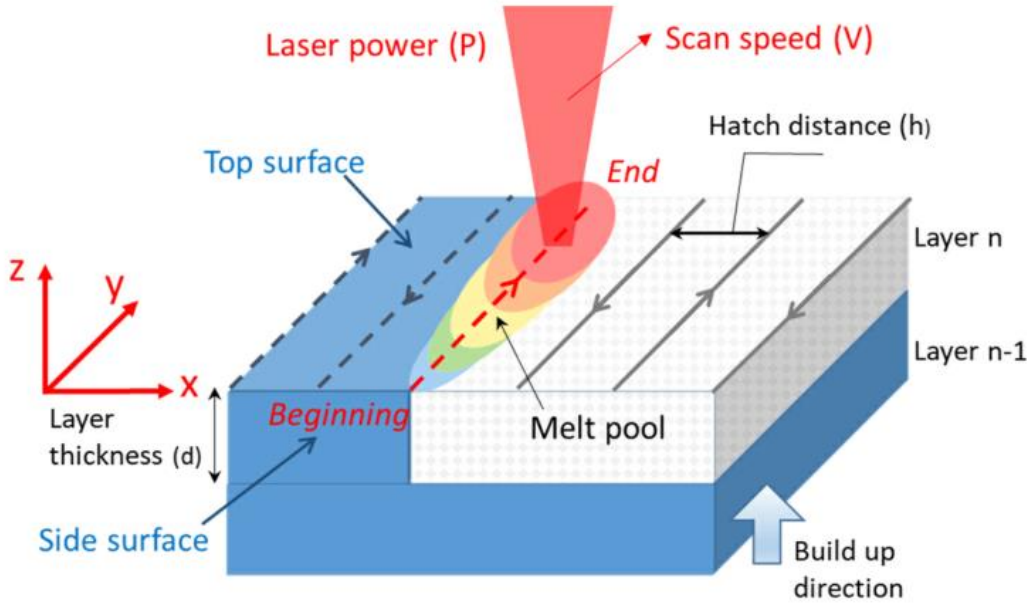

Fig. 3. Volume formation in the LPBF process and corresponding surfaces generated.

In industrial implementations, parts are characterized by high precision, high reliability, and long fatigue life, so the surface morphology of the parts obtained by metal AM techniques often does not meet these high requirements [Tian Y, Tomus D, Rometsch P, et al., 2017]. Although several post-processing procedures can improve the performance of components produced by AM techniques, these approaches increase time and production costs, resulting in increased expenses and poor cost effectiveness for the industry [Leon, Avi, and Eli Aghion, 2017]. In reality, because to the limits that different treatments might have on the ensuing contact between the exterior (lattice structure) and interior (channel) surfaces, direct application to minimize surface roughness is not always reliable. It has also been demonstrated that the part surface may stay as built from AM or even cause the part function to deteriorate [Stimpson, C. K., Snyder, J.

C., Thole, K. A., and colleagues, 2016]. The pressure drops in components with narrow tortuous cooling channels, for example, are substantially influenced by the surface roughness of the sides [Nagalingam, Arun Prasanth, and S. H. Yeo, 2020].

Therefore, the goal of determining the best measuring methodology for metal AM is to improve both manufacturing control and the quality of printed items.

1.3 Measurement Methodology in LPBF process

Numerous features defining tolerances (geometric product standards as established by the International Organization for Standardization) must be taken into consideration while designing components for AM. In order to confirm that the part's features adhere to the tolerance range specified by the design, several measuring techniques are applied in various manufacturing scenarios. In contrast to other traditional production methods, AM gives designers a greater degree of latitude when creating intricate interior structures. This capability allows for the creation of geometries that are not possible using conventional machining methods since AM does not block access to the tools of most manufacturing methods [Ian Gibson, Ian Gibson. 2015]. However, as was previously indicated, given the numerous process and environmental factors that influence the LPBF process, it is challenging to forecast and manage the process outcome (final material properties, surface and dimensional features of the component, etc.) [Campbell, Ian, David Bourell, and Ian Gibson, 2012].

Trial-and-error techniques have hit their limit in terms of the quality of components produced by metal additive procedures. In-situ monitoring signatures of the process is essential to overcoming this restriction [Mani M, Feng S, Lane B, et al. 2015]. In-situ process monitoring,

which allows for simple access to each layer of the printed structure and quantifies the correlation of elements relating to the print process outcome, has grown in popularity as research into LPBF has progressed. As measuring system equipment, the majority of these research relied on high-speed, high-resolution cameras and projectors. The in-situ measuring systems used in the LPBF process are primarily classified into on-axis and off-axis systems. More and more research is concentrating on in-situ metrology methods in AM to measure the development of the powder bed and the cured zone after melting.

Real-time monitoring enables us to incorporate potential feedback control systems to make up for or repair problems that have been noticed, or to stop producing defective components altogether. Such as illustration by designing and adding full-state-feedback controllers to obtain the entire spatial profile of the melt pool temperature and moving interface position [Koga, S., Krstic, M., & Beaman, J. 2020]. Our understanding of the physics behind the additive process will expand thanks to in-situ measurements, which will also hasten the development of the method, leading to better material and structural qualities. Thermal imaging and high-resolution optical imaging have received a lot of attention in studies on in situ metrology of LPBF process.

In an in-situ monitoring experiment using AlSi10Mg as the printed material, faults over 50 μm may be monitored nearly entirely by a successful IR detection and data processing technique, while monitoring of minor defects below 50 μm may need an improvement in IR spatial resolution or a change in camera orientation to enhance its accuracy [Estalaki S M, Lough C S, Landers R G, et al. 2022]. High-resolution optical imaging enables the defect monitoring range to be decreased in comparison to the IR thermographic technique such that the range resolution of the monitoring fits the corresponding defect size.

To solve the problem of minimizing surface topographical roughness, we must regulate the settings while monitoring the printing process. A newly developed fringe projection technique can measure a print area of 110 x 150 mm on an Inconel 718 powder bed and achieve vertical resolution requirements of at least 40 μm and lateral resolution requirements of 38 μm [Zhang H, Vallabh C K P, Xiong Y, et al. 2022].

The previously reviewed literature uses high-resolution optical systems, which means that capturing higher-quality morphology comes with corresponding optical problems. During metal AM, specular reflections from the printed surface can lead to loss of discernable field of view and can have a significant impact on the accuracy of fringe pattern-based measurement methods. Therefore, in this work, we aim to improve the in-situ FPP measurement method for metal AM by using more phase steps and adding polarizers to mitigate the issue caused by the highly reflective surface topography measurements.

2.0 Fringe Projection Profilometry

The non-contact measurements made possible by optical 3D shape measuring techniques make them crucial for use in industrial, medical, and biometric applications. Structured light approaches, when compared to other techniques, have the benefits of high resolution, full-field assessment, and speedy data capture. Structured light 3D measuring techniques include optically based 3-D contour measurement. One of the most popular methods for measuring 3D shapes is fringe projection profilometry (FPP), which reliably extracts 3-D shape data from the striped pattern that is projected onto a 3D object's surface. The FPP method is one of the free irregular plane measuring techniques that are especially ideal for high resolution due to the advantages of comprehensive detection, high response, high resolution, and accuracy.

The main components of a FPP system are a projector and a camera. The projector projects a series of various fringe patterns with sinusoidal variations onto the surface of the measuring object, and after a number of calibrations, the camera captures these fringe patterns from various angles. The projected fringe patterns can be deformed by variations in the height of the 3D object surface, and these distorted fringe patterns are then reconstructed to get the 3D structure of the measurement object.

2.1 Fringe Projection Profilometry Utilization

One of the most active study topics in the field of optical metrology in recent years has been the creation of (3D) three-dimensional surface information utilizing fringe projection

methods [Gorthi S S, Rastogi P. 2010]. The ability to retrieve an object's 3D form is of great interest. It has considerable potential for use in a variety of fields, including industry, technology, medicine, and heritage protection [Chen F, Brown G M, Song M. 2000]. The use of coordinate measurement machines (CMMs) is widespread and well-established in several applications. CMMs do, however, have certain drawbacks, including expensive price, slow measuring speed, and few measurement spots [Martínez A, Rayas J A, Puga H J, et al. 2010].

In the field of biomedicine, optics-based phasor measurements have been widely used. Multi-frequency five-step phase shifting fringe patterns were generated in a DMD projector and projected onto the surface of animal viscera considered as human organ structures, and the phase unfolding process was avoided by a peak-seeking algorithm to obtain organ 3D shapes [Jiang C, Jia S, Xu Y, et al. 2015]. By calibrating the geometric lens distortion in the projection and imaging channel optics, the endoscope uses FPP to add an additional depth dimension to standard 2D otoendoscopic images of the ear and can be used as a non-invasive technique to extend the qualitative depth perception of the clinician with quantitative 3D data of the surface of the tympanic membrane [Muyshondt P G G, Van der Jeught S, Dirckx J J J. 2022]. To address the increased complexity of traditional fluorescent markers for suturing systems as well as safety concerns, landmark heat maps were regressed from four channels of FPP-generated data using the adopted U-Net, developed as a 3D vision system using FPP to assist in robotic surgery and autonomous suturing [Wei S, Kam M, Wang Y, et al. 2022].

In the AM-related field, the structure and characteristics of powder bed layers, including and not limited to flatness, surface texture, average descent height, and surface feature Length, were measured in situ during the manufacturing process by implementing a digital fringe projection technique [Zhang B, Ziegert J, Farahi F, et al. 2016].

2.2 Motivation and Objects for Improving Fringe Projection Profilometry in LPBF process

The ZIP-AM lab at the University of Pittsburgh designed and constructed the in-situ FPP measurement research system on top of a commercial LPBF machine as shown in Fig. 4.

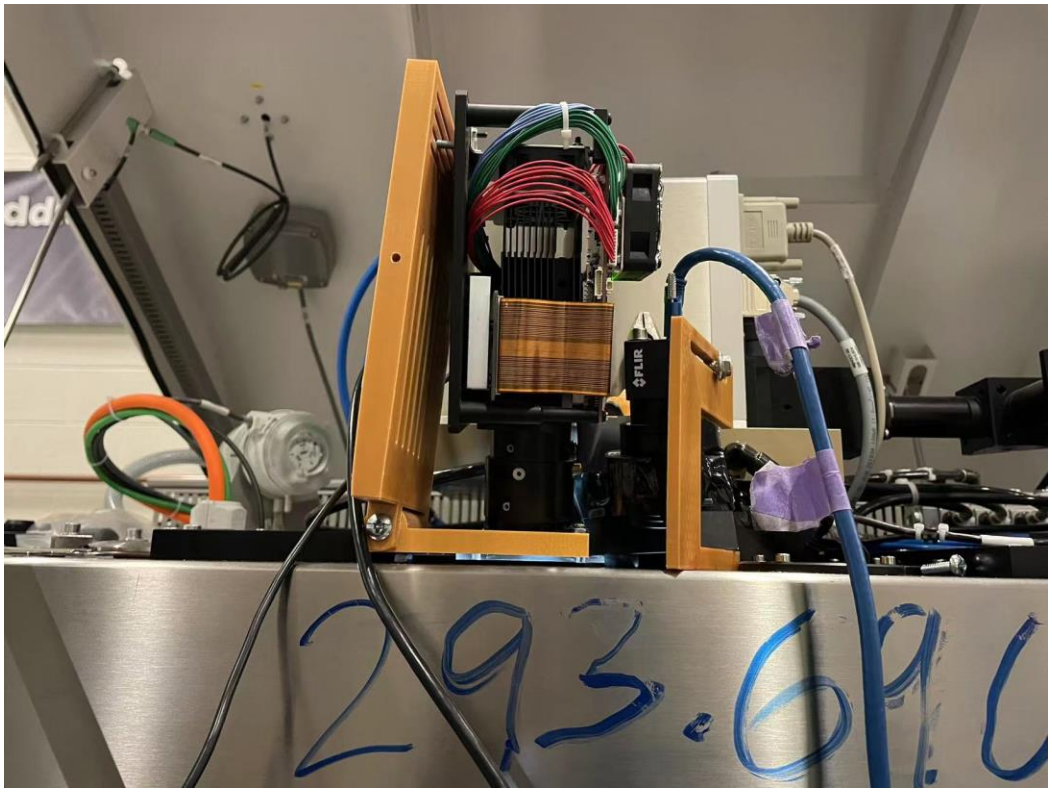

Fig. 4. The schematic of in-situ FPP system in ZIP-AM lab (University of Pittsburgh) .

The fundamental operation of LPBF is to lay down the powder, fuse it, frame it, and then duplicate it layer by layer, as we mentioned in Section 1.1. The flat surface of the powder bed is therefore crucial for LPBF printing and is directly related to the final mechanical properties of the part. However, there are a number of unpredictable faults in the LPBF process that can cause the thickness of each layer to diverge from the preset value (e.g., melt pool spattering, varying powder melting rates, and other forms of porosity consequences). Because these flaws cause inconsistencies in layer thickness, which impact the ultimate surface roughness, it's critical to use

precise process monitoring. During the LPBF process, the camera and projector based FFP approach may be used to assess the efficiency of the powder bed and the geometric accuracy of the surface. At the same time, this vision-based metrology method partially addresses the AM quality control challenge, but the capacity to describe 3D structures with extremely high spatial resolution across relatively wide regions is what is most needed (up to a few centimeters square). [S. K. Everton, M. Hirsch, P. Stravroulakis, and others, 2016].

In the LPBF process, since it is formed by melting metal powder, the reflection on the surface of the printed object is divided into specular reflection and diffuse reflection. As shown in Figure 5, the specular reflection component on the surface of the LPBF object is larger than the diffuse reflection component. Since the saturated area of specular reflection can completely block any fringe pattern, it can lead to the loss of depth information.

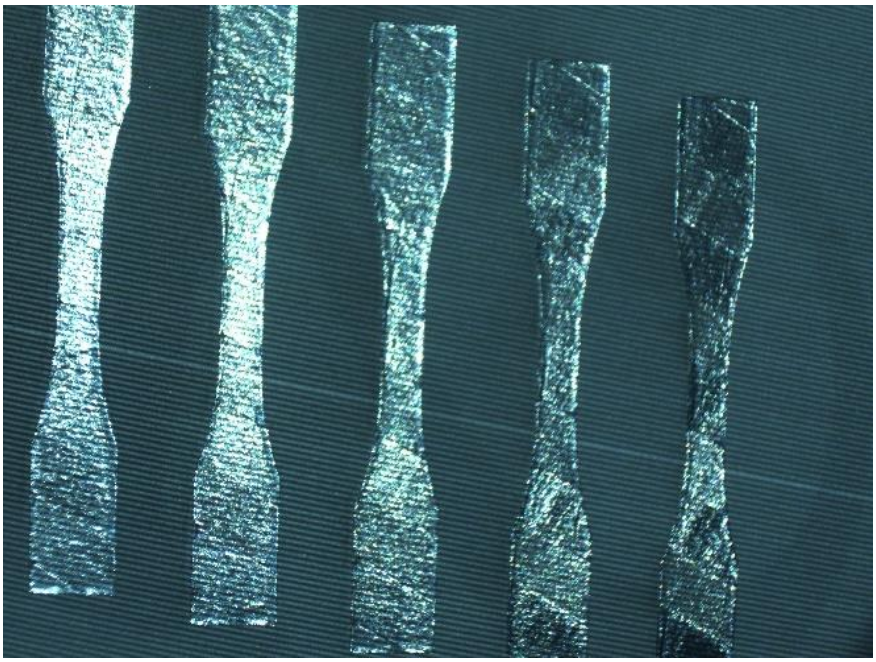

Fig. 5. One layer image of fatigue test bar during LPBF printing process with fringe patterns

Although the effects of different phase shift algorithms on the calibration methods of linear inverse phase height model, polynomial phase height model and equation-based phase height model with control equations are similar. But their calibration accuracy can be improved by a phase shift algorithm with a large number of steps [Feng S, Zuo C, Zhang L, et al. 2021]. By adding extra phase-shifting steps to the FPP system, an attempt is made in this study to improve the method's accuracy on metal surfaces with high reflectivity. The corresponding experimental results are obtained by comparing the experimental results of the conventional 3-step phase shift method with those of the 12-step phase shift method. Using these results, we investigate whether the accuracy of the experiment can be increased by altering the number of phase shifts. At the meantime, to handle objects with highly reflective shiny surfaces, a polarizing filter is used to eliminate the effect of high light by changing the angle between the transmission axes of the polarizer. Intense specular light is effectively removed; however, at the cost of reducing the captured intensity of the entire image, which can result in a low signal-to-noise ratio [Umeyama, Shinji, and Guy Godin. 2004].

The next section focuses on the physics underlying the FPP approach and the enhanced in-situ monitoring system at the ZIP-AM lab at the University of Pittsburgh. We will investigate and explain how increasing the phase steps and adding linear polarizers can be used in FPP methods to improve the in-situ measurement performance.

3.0 Proposed methods to Improve Fringe Projection Profilometry for LPBF monitoring

As illustrated in Figure 6, a typical FPP system comprises of a computer, a projector, a reference plane, and a camera. A fringe pattern generated by a computer is projected onto the item, and because of the geometry of the object, the camera records the distorted fringe pattern. When determining the real height of a 3D object, the reference plane serves as the reference height. The following are the essential steps in measuring 3D features via fringe projection:

(1) Project a series of computer-generated predefined fringe patterns (usually sinusoidal variation fringes) onto the measured target surface through a projector.

(2) On the surface of the object, the fringe patterns are distorted and reflected by the surface morphological structure. The main sources that make up its reflected light are the projector light source and the ambient light source, and the object modulates and reflects the stripes with the ambient light. The camera captures the projected fringes distorted by the change in height of the object's surface and performs transformations such as inverse trigonometric functions to evaluate the amount of distortion in terms of phase values.

(3) Due to the discontinuity of the inverse trigonometric function, a continuous phase map on the target plane that is positively associated with the height map may be produced using a phase expansion procedure such as the reference guided + two-dimensional Fast Fourier Transform (2D FFT) approach.

(4) Using a calibration system that corresponds to various height phases with plane center coordinates to transfer the unfolded phase maps into the realistic coordinate system.

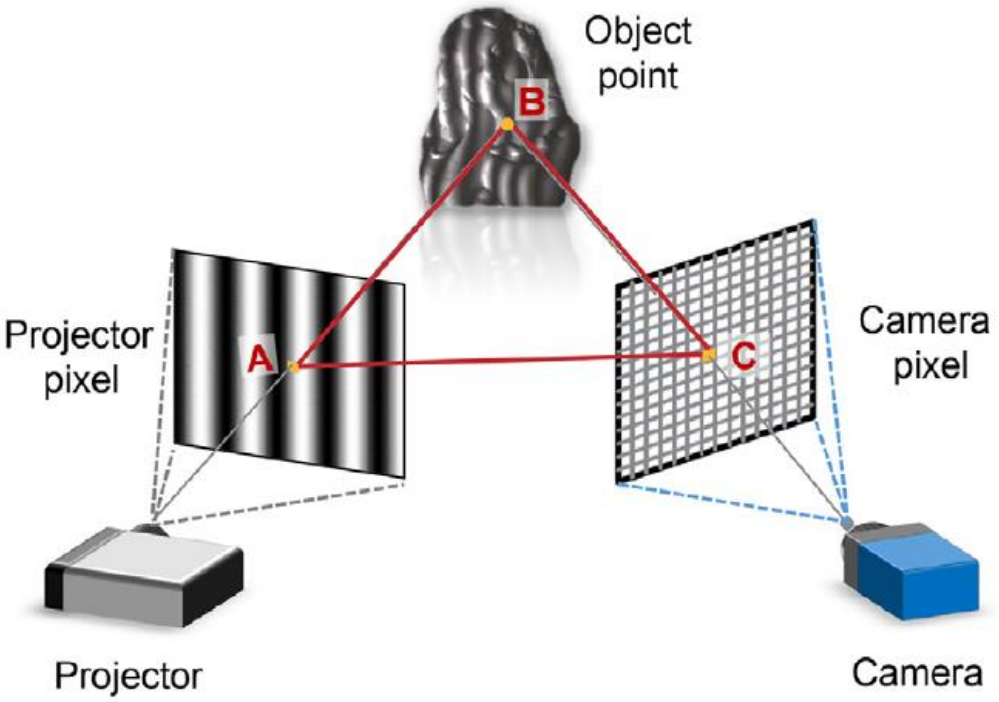

Fig. 6. The layout of fringe projection profilometry system.

3.1 Geometric Model in Fringe Projection Profilometry

Since neither the camera nor the projector are parallel to the surface of the item being measured, as was stated in Section 2.2, the surface characteristics of the object may contribute to the height difference between the reference plane and the surface of the object. The spatial distribution of the corresponding fringe phase values and fringe intensity determines the dimensional information of each pixel point located on the surface of the measured item.

In order to get measurements with a high degree of precision, the fringe projection system needs to be calibrated. A phase-to-height conversion in the vertical direction and an intensity conversion between the fringes collected by the camera and the fringes projected by the projector

are the two objectives of calibration [Zhang B, Ziegert J, Farahi F, et al. 2016].. The first step is known as $K(x,y)$ calibration, which adequately reflects how sensitive the phase change is to height. The second process is called $C(x,y)$ calibration, and this correction factor combines the effects of object surface reflectance and projector nonlinearity to correct the intensity relationship between the projector and camera center pixels [Zhang H, Vallabh C K P, Xiong Y, et al. 2022].

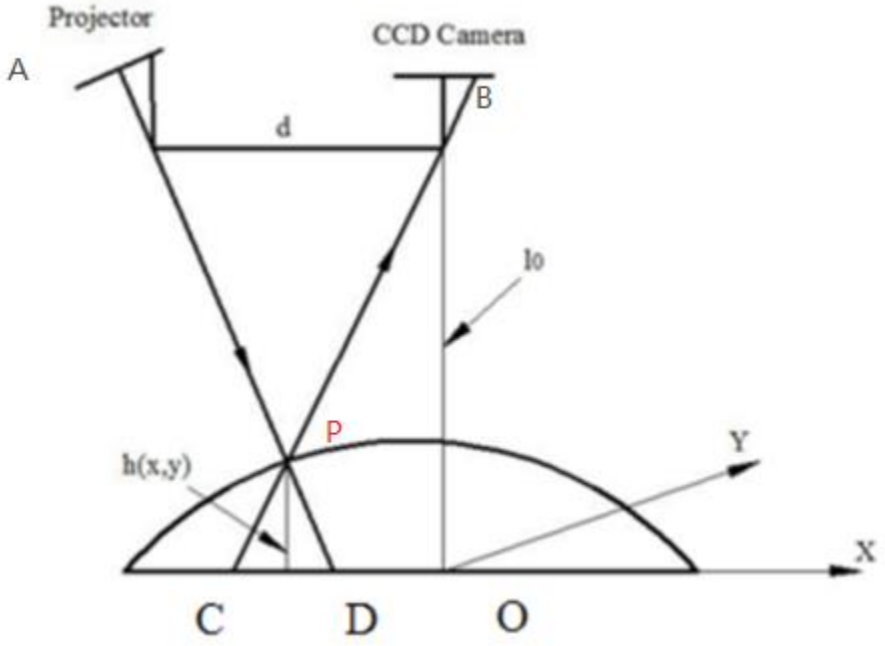

Fig. 7. The geometrical relationship of the fringe projection system.

The association between the FPP system and its mathematical geometric model are shown in Figure 7, where $h(x,y)$ represents the surface height of the object measured at point P, d represents the distance between the CCD camera and the projector, and l_0 represents the distance between the CCD camera and the reference plane. On the reference plane, a fringe of a certain intensity is projected from point A to point D by the projector, and the reflected pattern and beam are recorded by the CCD camera at point B. The beam is actually recorded by the camera at point

P because the surface characteristics of the measuring item will be higher than the reference plane. Since the projected stripe pattern is derived from the sine wave variation, the relationship between $\overline{CD}$ and phase variation $\Delta\varphi(x,y)$ can be expressed as equation (3-1)：

$$\Delta\varphi(x,y) = 2\pi f \cdot \overline{CD} \qquad (3-1)$$

where *f* denotes the frequency of the sine function of the fringe pattern and is the inverse of the length of the distance between two adjacent stripes of the projection. In the case of known $\overline{CD}$, the relationship between d, l_0 and $h(x,y)$ is deduced using the similarity ratio theorem of triangles, and the mathematical expression and the derivation process are expressed as (since $\overline{CD} \ll d$):

$$\frac{l_0 - h(x,y)}{h(x,y)} = \frac{d}{\overline{CD}}, \rightarrow h(x,y) = \frac{l_0 - h(x,y)}{d}\overline{CD} \qquad (3-2)$$

$$h(x,y) = \frac{\overline{CD} \cdot l_0}{d + \overline{CD}} \rightarrow \frac{\overline{CD} \cdot \frac{l_0}{d}}{\frac{d + \overline{CD}}{d}} = \frac{\overline{CD} \cdot l_0}{d} \qquad (3-3)$$

Bringing the relationship of $\overline{CD}$ to phase change $\Delta\varphi(x,y)$ into Equation (3-3), we can obtain a simplified equation for the height of the object being measured:

$$h(x,y) = \frac{l_0}{2\pi f_0 d} \cdot \Delta\varphi(x,y) \qquad (3-4)$$

The aforementioned proof is predicated on the observation that the coordinates of points A, B, C, D, and P are in the same plane that is perpendicular to the x-axis, as shown in Figure 7. However, in the actual measurement procedure, l_0 will be extended laterally, which is essentially a coordinate function $L(x,y)$ that changes depending on where the pixel is located. Therefore, contrasted with l_0 as a constant, we rewrite equation (3-4) to get a new formula for the height of the observed item as [Zhang H, Vallabh C K P, Xiong Y, et al. 2022]:

$$h(x,y) = K(x,y) \cdot \Delta\varphi(x,y) \qquad (3-5)$$

$$K(x,y) = \frac{L(x,y)}{2\pi f_0 d} \qquad (3-6)$$

3.2 Basic Wrapped Phase Calculation Method

As shown in Figure 7, Point C is the comparable location of the uniform fringe pattern reflected off the measuring object surface, whereas Point D is the position of the fringe pattern on the reference plane. Because of this, the fringe pattern is distorted due to the surface of the item in the measuring region. Equation (3-7 & 3-8), respectively, contains the mathematical expressions for the fringe pattern intensity of the object surface and the reference plane:

$$P(x,y) = I_0(x,y) + M(x,y) \cdot \cos[2\pi f x + \varphi_P(x,y)] \qquad (3-7)$$

$$I(x,y) = I_0(x,y) + M(x,y) \cdot \cos[2\pi f x + \varphi_I(x,y)] \qquad (3-8)$$

in which $I_0(x, y)$ denotes the background average intensity, $M(x, y)$ denotes the fringe patterns' modulation, φ_P denotes the phase that is impacted by the object's height, φ_I denotes the reference plane's phase, $P(x, y)$ denotes the deformed fringe pattern on the surface of the measured item, and $I(x, y)$ denotes the fringe pattern that is reflected by the reference plane.

Equation (3-5) shows that the FPP system needs the value of phase change as an input to get the height of the corresponding pixel point. From equations (3-7 & 3-8) we can obtain the value of the phase change $\Delta\varphi(x, y)$, whose expression is as follows：

$$\Delta\varphi(x, y) = \varphi_P(x, y) - \varphi_I(x, y) \qquad (3-9)$$

The fringe analysis method, which contains the phase shift and the decoupling algorithm, is at the foundation of the fringe projection technique in order to precisely determine the value of the phase change of the patterns from the pictures taken by the camera. Here, we utilize the least square phase shift technique to translate the pixel intensities in the acquired image into the associated phase values [Creath K, Wyant J C. 1992]. Each frame of the projected fringe pattern has an initial phase, and starting with the following frame, the pattern is displaced by $\frac{2\pi}{N}$ from the previous frame. It incorporates N frames of sinusoidal patterns projected onto the surface of the measuring object. The accuracy of this technique may often be increased by adding more phase steps because it is intended to decrease the phase error. A number of sinusoidal fringe patterns are projected on the surface of the item while the digital fringe projection system is in operation. The pattern's irradiance distribution for each pixel (*x, y*) is written as：

$$I_i(x,y) = I_0(x,y) + M(x,y) \cdot \cos[\varphi(x,y) + \delta_i] \qquad (3-10)$$

where $I_0(x,y)$ and $M(x,y)$, the background intensity and intensity modulation of the fringes, respectively, have been previously introduced; i is the number of frames; δ_i signifies the phase-shifting step of the subsequent two frames of the stripe pattern; $\varphi(x,y)$ is the phase value of each pixel point; and the phase-shifting step δ may be represented as

$$\delta_i = \frac{i}{N} 2\pi, i = 1, \dots, N \qquad (3-11)$$

In Equation (3-10), the phase value of the fringe pattern captured by the CCD camera through the phase-shift algorithm is the wrapped phase φ, and the following is the extraction formula of the wrapped phase map：

$$\varphi(x,y) = \tan^{-1} \frac{-\sum_{i=1}^{N} I_i(x,y) \cdot \sin\left(\frac{2\pi i}{N}\right)}{\sum_{i=1}^{N} I_i(x,y) \cdot \cos\left(\frac{2\pi i}{N}\right)} \qquad (3-12)$$

This formulation is also a special case of the least squares method, which is the basic equation for all standard N-step phase-shifting techniques when the streaks of the phase-shifted pattern are equally spaced within a 2π period. The phase shifts of the stripe patterns need not be consistent in typical N-step least squares algorithms and can instead be dispersed across a range

bigger than 2π [Greivenkamp J E. 1984]. Another important issue is the finite phase range resulting from the arctan function in Equation (3-12). It should be noted that a straightforward application of the arctan function only yields the value of phi in the interval $-\pi/2$ to $\pi/2$, or a range of π. The four-quadrant tangent may be used to resolve sign ambiguity in the numerator and denominator and to compute the phase value at each point modulo 2π in real computation process. This phase-shifting algorithm is only concerned with the retrieval of wrapped phases. Phase unwrapping is necessary to generate a continuous or absolute phase map since the wrapped phase map $\varphi(x, y)$ has a discontinuity modulo 2π.

In this work, the first proposed approach for improving FPP in LPBF monitoring is to increase the phase step number N from current 3 to 12. Details are presented in Section 4.1.

3.3 Improved Wrapped Phase Calculation using Localized Corrected Camera Intensity

The FPP system made up of a camera and a projector is a not proportional system, and the intensity of the light source projected by the projector is usually nonlinearly related to the image captured by the camera. In the phase unwrapping calculation, the phase captured by the camera has harmonic errors with the actual profile height of the target object [Xiong, Yubo. 2021]. From Fig. 7 we can learn that to determine the height information $h(x, y)$ of the object, it is necessary to extrapolate from the FPP model to calculate the spatially shifted distance of the fringe patterns. In other words, the phase change $\Delta\varphi(x, y)$ in the reflected light field from the surface of the target object captured by the camera is directly related to the projected fringe spatial shift $\overline{CD}$.

Each image captured by the camera in the LPBF process its inherent image pixels are related to several parameters and are functionally related. The specific functional expression is as follows [Zhang H, Vallabh C K P, Xiong Y, et al. 2022]，

$$I_{camera}\,(x,y) = I_{projector}\,(x,y) \times R(x,y) \times Q(x,y) \qquad (3-13)$$

where (x,y) denotes the coordinates of the each pixels, and the pixel point intensity is the intensity $I_{camera}\,(x,y)$ captured by the camera, the source intensity $I_{projector}\,(x,y)$ from the projector, the reflectance $R(x,y)$ of the target object surface and the ratio of input to output (for called camera's sensor response) $Q(x,y)$. Since the material used for the target object and its surface properties change with coordinates and position relative to the camera, R varies spatially. Q itself varies spatially with the projection of the surface intensity and the camera captures the intensity nonlinearly, so it can be rewritten as $Q_{xy}\left[Q_{camera}\,, Q_{projector}\right]$, where the parameters represent the nonlinear variation of the projector and the camera, and equation (14) is rewritten in the following form:

$$I_{camera}\,(x,y) = I_{projector}\,(x,y) \times R(x,y) \times Q_{xy}\left[Q_{camera}\,, Q_{projector}\right] \qquad (3-14)$$

Numerous studies and results have demonstrated that the R and Q are homogenized by the FPP approach currently used for LPBF process monitoring. Despite the fact that this assumption does not fully reflect the camera sensor's nonlinear fluctuation, it simplifies phase assessment. By altering the wrapping phase computation and adding a local correction for the brightness of the

camera-captured pictures, a more precise phase assessment approach for FPP in lpbf processes is created. Equation (3-14) is rewritten to derive the correction factor Cxy, which is then combined with the nonlinear effects of surface reflectivity and the projector camera. This correction factor may be expressed succinctly as ratio of $I_{projector}\,(x,y)$ and $I_{camera}\,(x,y)$ [Zhang H, Vallabh C K P, Xiong Y, et al. 2022].

$$I_{projector}\,(x,y) = \frac{I_{camera}\,(x,y)}{R(x,y) \times Q_{xy}\left[Q_{camera}\,, Q_{projector}\right]} = \frac{I_{camera}\,(x,y)}{C_{xy}} \qquad (3-15)$$

$$\frac{1}{C_{xy}} = \frac{I_{projector}\,(x,y)}{I_{camera}\,(x,y)} = \frac{1}{R(x,y) \times Q_{xy}\left[Q_{camera}\,, Q_{projector}\right]} \qquad (3-16)$$

The calibration procedure makes it more challenging to track the projected source intensity in real-time basis, thus we calculated the correction factor by projecting a number of pictures with equal intensities onto the plane using the projector. We chose to project 18 uniform grayscale images ($I_1 = 0$, $I_2 = 15$,…, $I_{18} = 255$, as shown in Fig. 10) of equal intensity from 0 to 255 onto a flat print powder bed (the target print object will be used as the print reference surface) for the experiment because the CMOS camera we used for the experiment has an 8-bit digital output and we need to keep the projected intensity within the sinusoidal fringe intensity range. We establish a ratio of the two nonlinearities by fitting the intensity of the plane that the camera captures to the intensity that the projector projects. Each pixel point has a matching C_{xy} correction factor function by constructing the same function matrix as the resolution of the camera-captured picture (CMOS camera captured image resolution is 3000×4000).

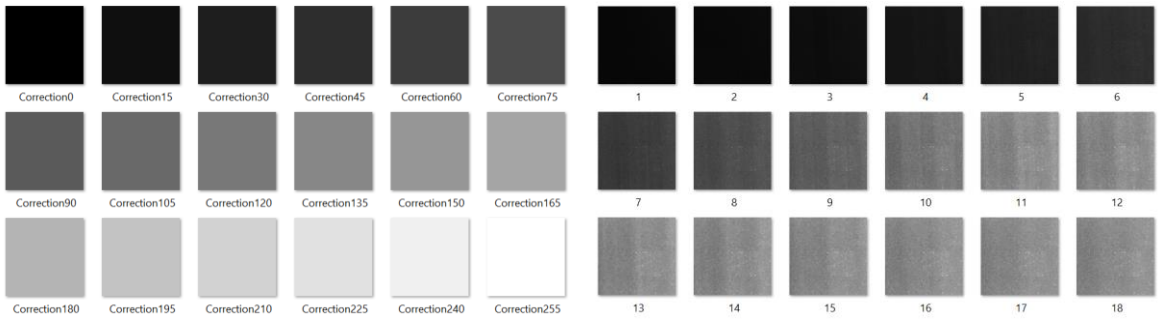

Fig. 8. Intensity images from projector and camera.

It is obvious that the value of C_{xy} fluctuates greatly with the position of the measured pixels by comparing the correction factors for various pixel positions in the photos. We chose the C_{xy} curves in the center coordinates and four edge coordinates for fitting (shown in Fig.11), and by comparing the goodness of fitting (GoF) of the C_{xy} curves for five different points, that is, the R-square (R^2) values of the respective fitted curves, it is more obvious that the FPP method's accuracy needs to be improved by including specific pixel point correction factors.

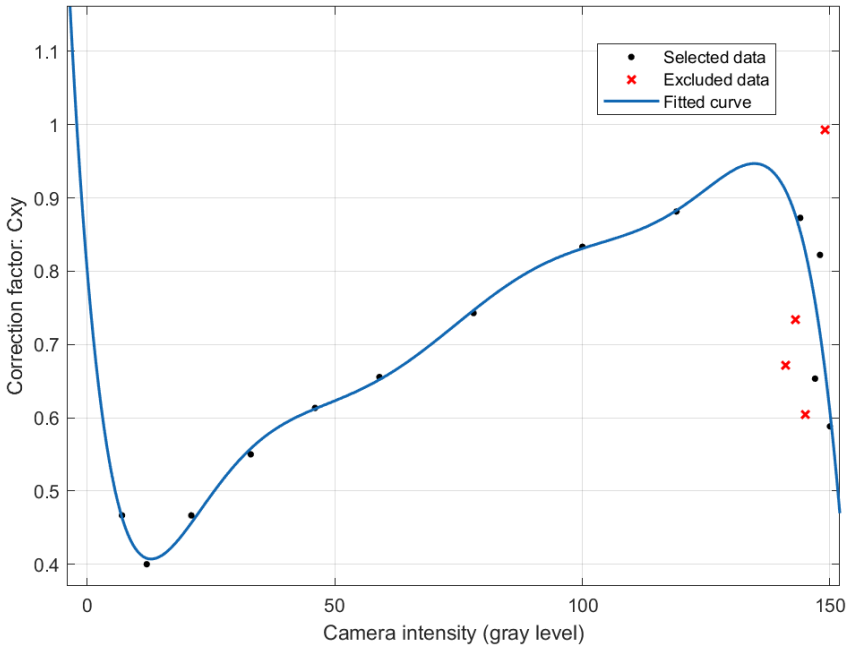

Fig. 9. C_{xy} calibration regression result from center coordinates.

3.4 Phase-to-Height Mapping via Localized Experimental Calibration

3.4.1.1 Lateral Pixel-to-Length Calibration

Since the projector and the camera have a specific angle in the experiment and the optical axis of the camera is not defined perpendicular to the printed powder bed, we need a direct pixel to length (millimeter) transformation process through a lateral calibration. This calibration method is first achieved using an external calibration grid plate tool with precise measurement dimensions. In the experiment, a fixed size grid plate is placed on the print bed and mapped by comparing the coordinates on the grid plate and the pixels of the non-orthogonal patterns taken by the CCD camera. The grid spacing is determined in pixels, thus establishing a relationship between the image pixels and the millimeter units of the grid spacing.

For each experiment a perspective calibration was required to match any alignment changes in the actual experimental setup. The projection change matrix T created by calibrating the shot can be expressed as a 9 × 9 matrix with the expressions

$$[x', y', z'] = T_{9\times9}[x, y, z] \qquad (3-17)$$

where x, y, z denote the coordinates of the plane object in space [Wolberg, George. 1990], respectively. The ratio of pixels to millimeters in x-y coordinates can also be determined by calculating the number of pixels for a known square grid length, as shown in Fig. 9. In this experiment, the size of the actual square grid is 5 mm × 5 mm, which corresponds to 40 μm × 40 μm pixels.

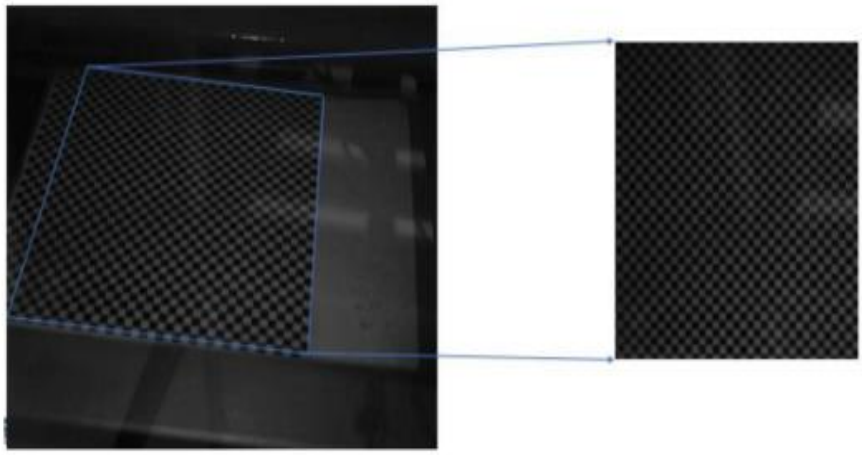

Fig. 10. In-plane pixel-to-length calibration artifact.

3.4.1.2 Vertical Phase-to-Height Conversion

In equation (3-5), we obtain a simple expression for measuring the height of an object, so in order to be able to improve the performance of the FPP method-based in situ monitoring technique in the LPBF process, we need to analyze the term $K(x, y)$ which we have discussed formerly. In the current study, most researchers prefer to use the constant K as the coefficient value of the whole measurement plane than using the spatial resolution $K(x, y)$. From Equation (3-5), we can intuitively calculate $K(x, y)$ by using the corresponding parameters l_0, d and f, which can reflect the sensitivity of the phase change value to the measured height. To obtain an accurate relationship between the phase and height values, we perform an experimental calibration of the out-of-plane unpacked phase-height conversion by using a least-square calibration method, also

called effective wavelength calibration. In the LPBF process, the unwrapped phase map of the plane is obtained by using a phase shift and phase unwrapping process to shift the flat plane after spreading the powder within a certain height range (covering the height variation of the powder bed) by a fixed value. In our present experiment, we take the first powder layer as the reference plane (defined height position of 0mm) and make the construction platform move around the nominal height of the powder layer ten times with each increment of 0.1mm, i.e. ten heights corresponding to defined heights of 0mm, 0.1mm, 0.2mm, ..., 0.8mm, 0. 9mm. these ten defined heights The unwrapped phase of each pixel of these ten defined heights is fitted to a straight line by a linear scale function, which is able to obtain the slope. As shown in Figure. 8, the upper panel shows the $K(x, y)$ calibration map across the field of view, and the lower panel shows the straight line fit curve of the center pixel of the unwrapped phase map for each layer.

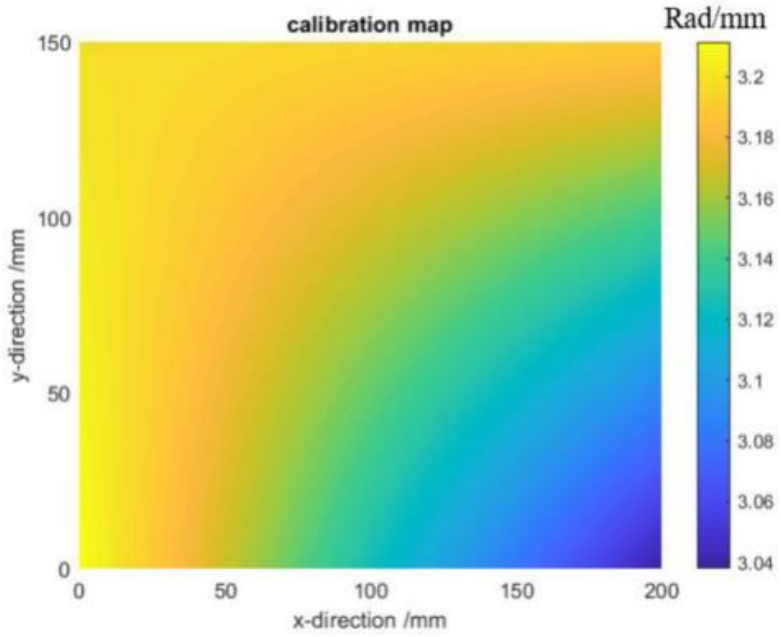

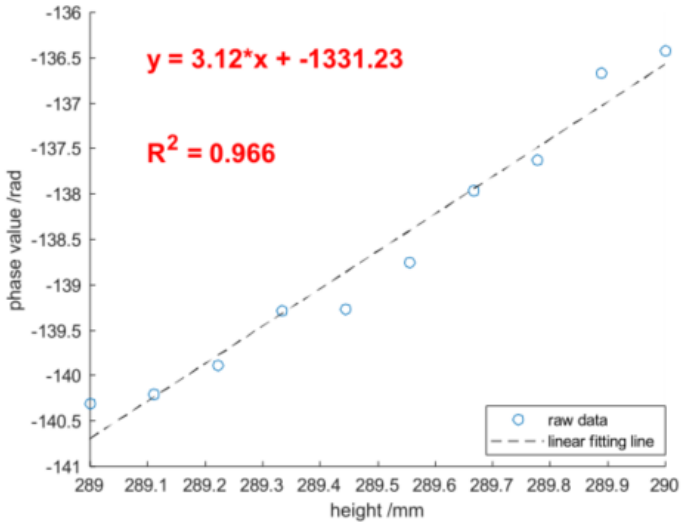

Fig. 11. $K(x, y)$ map and straight-line regression coefficient sample.

It is essential to provide calibration variables to the kxy calibration after the C_{xy} calibration is finished because the camera capture intensity during $K(x, y)$ calibration is likewise directly connected to its correctness. As a result, the whole calibration procedure uses perspective calibration to complete the $K(x, y)$ calibration before introducing all calibration parameters into the FPP code for the phase unwrapping process. C_{xy} calibration serves as the nonlinear intensity calibration throughout the entire process.

3.5 Applying Linear Polarizers to Improve FPP

In photographic vision, the "glare" or "shine" reflected from a light source can affect the image processing results when shooting objects with high reflectivity. These saturated portions

(also called overexposed areas) are often dealt with by using a polarizer as a countermeasure so that the light from the subject of the projector must be imaged on the image sensor. According to the law of reflection, the light projected by the projector will reflect on the surface of the object (i.e., the reflective surface) and will eventually become two types of reflected light: the first is light in the same state of incidence and reflection, i.e., specular or regular reflection; the other is diffuse or irregular reflection. For vision and camera imaging, the reflected light in the specular reflection state is identified as the light source of the projector itself. When specular reflection is more dominant, the high-light areas on the surface of the measured object are perceived by the camera sensor. A polarizer is an optical filter that allows only light polarized in a specific direction to pass through. Light passing through a polarizer is light that has electromagnetic waves in only one specific direction, where the direction of the electric field vibration of linearly polarized light is constant. By taking advantage of the properties of the polarizer, as shown in Figure 12, the addition of a polarizer to the original optical system can eliminate or reduce the harmful glare portion caused by the reflection of the light source. This optical arrangement eliminates the reflection of the light source on the subject caused by specularly reflected light (linearly polarized light) and allows only diffuse reflected light (non-polarized light) to be well imaged on the camera sensor.

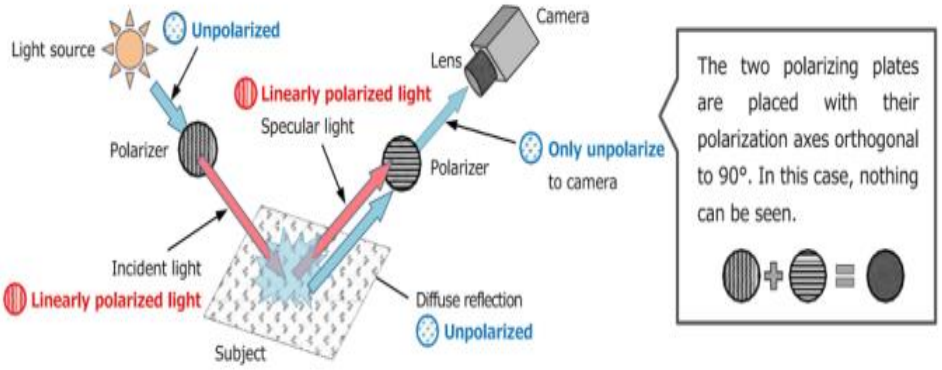

Fig. 12. Schematic diagram of the principle of extinction of visible light by polarizers [Toshiba Teli Corporation. 2020].

The most crucial aspect of the FPP approach is the camera's ability to record the fringe patterns that are reflected from the test object's surface for data processing, as was discussed in Section 2.2. As a result, the accuracy of the FPP approach is directly correlated with the integrity and clarity of the fringe pattern in the acquired image. The incident light that the projector projects onto the printed metal surface of the LPBF process is transformed into two types of reflected light (diffuse reflection and specular reflection), and the specular reflection will cause the loss of surface modulated fringes, which the camera cannot capture in full detail. Specifically, shiny parts' measurement has been a major challenge in optical metrology because of double-bounced light (a phenomenon where light can be reflected from one area of a surface to another surface). Unwanted light will result in higher noise in camera-captured images and can even make measurements' accuracy unacceptable [Hu Q, Harding K G, Du X, et al. 2005]. The second is that CCD cameras have a maximum intensity quantization level, once the intensity of light reflected from the specular region exceeds this level threshold, the camera's sensor reaches saturation and is unable to accurately collect any surface information. Some studies have shown that such effects can be eliminated by adjusting the exposure time of the camera, but since the adjustment of the

exposure time requires a lot of experimentation to cover the entire specular area of the measured surface in high light, it will increase the difficulty and time of calibration of the measurement process [Feng S, Zhang Y, Chen Q, et al. 2014].

Basel Salahieh, Zhenyue Chen et al. proposed a new multi-polarized fringe projection imagining technique algorithm that increases the visibility of the area by selecting different combinations of polarizer measurements and polarization angles to eliminate the saturation in the specular reflection region during the process of measurement. This algorithm provides a complete depth prediction of the object and a better reproduction of the measured object shape, allowing a more accurate reconstruction of the 3D shape of the object [Salahieh B, Chen Z, Rodriguez J J, et al.]

In this work, throughout the standard FPP system, we place a linear polarizer in front of the projector and camera lenses, respectively, to remove the effect of the specular reflection phenomena in the overexposed area on the FPP results, as was mentioned in the earlier introduction. After passing through the first polarizer in front of the projector, the incident light is transformed into linearly polarized light, and after being reflected on the measured plane, the original linearly polarized light transforms into a composite polarized light made up of the diffuse lobe, the specular lobe, and the specular spike. While the light in the diffuse reflection zone changes into light that vibrates in all orientations, the light in the specular reflection region maintains its linear polarization. The linearly polarized specularly reflected light is discarded after the composite light goes through the linear polarizer in front of the camera, leaving only the diffusely reflected light to be kept and photographed.

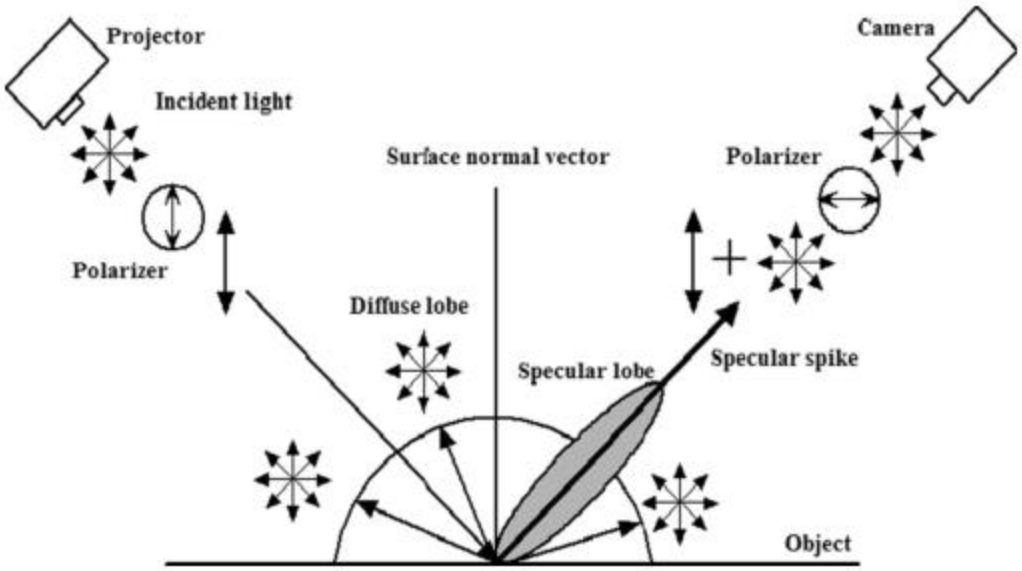

Fig. 13. Schematic diagram of a modified FPP system with polarizer intervention [Feng S, Zhang Y, Chen Q, et al. 2014].

The modified FPP system is shown in Figure 13, and the intensity of the final image captured by the camera through the whole process of light transformation we can define the expression consisting of specular reflection and diffuse reflection [Feng S, Zhang Y, Chen Q, et al. 2014]

$$I_C = I_{df} + I_{sp} = \frac{1}{4} I_P \alpha r_{df} + \frac{1}{2} I_P \alpha r_{sp} \cos^2 \theta \qquad (3-18)$$

Where I_{df} is the diffuse reflected light, I_{sp} is the specular reflected light, I_P is the intensity of the light source projected by the projector, I_C is the intensity of the image captured by the camera, α is the reflectance of the measured surface, and θ is the angle between the two polarizers placed in front of the projector and the camera.. r_{df} and r_{sp} represent the proportion of diffuse and specular reflected light in the composite light, respectively, and both satisfy r_{df}+r_{sp} = 1. For the

surface of the measured object where r_{sp} is much larger than r_{df}, we can simplify equation (3-18) and will obtain

$$I_C \approx I_{sp} = \frac{1}{2} I_P \alpha r_{sp} \cos^2 \theta \qquad (3-19)$$

Equation (3-19) teaches us that the angle θ between the linear polarizers is solely responsible for determining the intensity of the picture that the camera records. The camera cannot detect any fringe patterns in the FPP measurement when theta is equal to 90 degrees, meaning that the two linear polarizers are perpendicular to one another. This will have an impact on the subsequent pattern analysis. Thus, it is recommended that the angle between the linear polarizers not be adjusted to 90 degrees. Additionally, it shouldn't be much larger or much smaller than 90 degrees, since doing so would allow the camera's intensity I_C to be impacted by specular reflection, which will ultimately cause the camera's sensor to get saturated and cause the loss of streak patterns in the highlight region. We first set the angle θ in the experiment to 90 degrees, and then gradually rotate one of the polarizers to make the captured patterns in the camera clear until the pixels of the fringe pattern become saturated, in order to achieve a good linear polarization effect. This process allows us to determine the ideal polarization angle (45 degrees), which serves as the basis for the subsequent experimental replication.

3.6 Summary of the Modified Fringe Projection Profilometry Method with more Phase Steps and Polarization

The detailed procedures of the more-phase, polarization-aided FPP approach for LPBF process monitoring of high-reflectivity metals are summarized in flowchart 14. We accomplish this by projecting two sets of fringe patterns onto the reference and measurement target planes with different step phases (pi/3 and pi/12), respectively. Then, we use a CMOS camera to capture the original reflection images of the various phase-shifted images and the reflection images configured with linear polarizers, i.e., we obtain the unpolarized fringe reflection images and the polarized fringe reflection images. For each pair of phase images with a distinct phase shift, wrapped phase calculations were carried out independently. To increase the effectiveness of local pixel-level adjustments, the intensity calibration factor C_{xy} step of the projector-camera stated previously was also applied. Two sets of data (polarized and unpolarized) were also needed for the C_{xy} function since the linear polarizer influences the amount of light the projector projects and the camera records. For projector nonlinearity, camera sensor nonlinearity, and surface reflectance nonuniformity of the printed powder bed, Equation (3-17) simplifies these correction functions. The surface topographical height for the following phase deviation may then be determined by using the FPP system calibration (i.e., in-plane and out-plane calibration) to obtain the relevant *K(x, y)* values (same as C_{xy} for both groups: polarized and unpolarized). According to the experimental findings, the newly developed polarization FPP approach may lessen specular reflections during the detection process, and can thus satisfy the requirements for the LPBF process. Greater precision in situ monitoring to handle measurements of highly reflective metal surfaces.

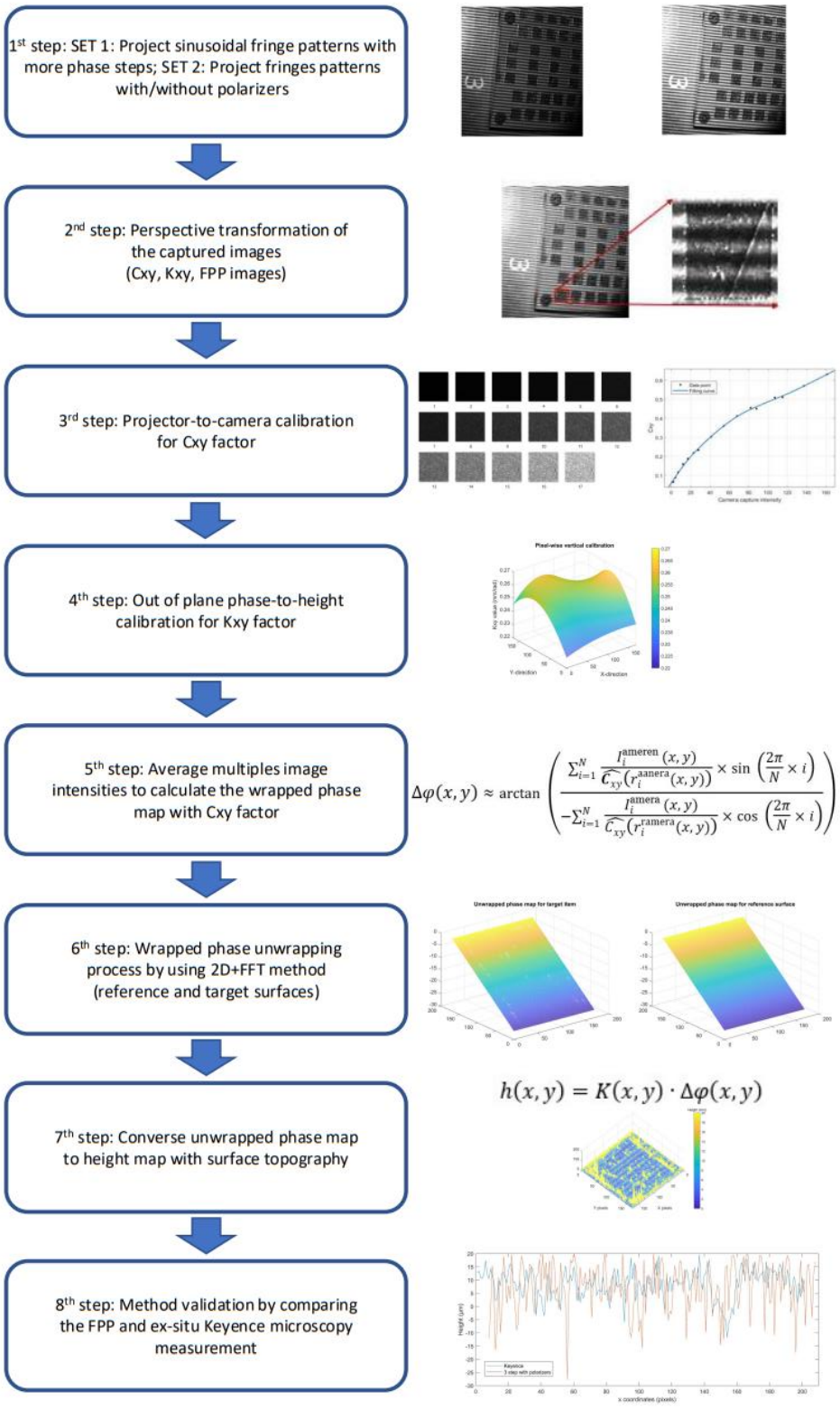

Fig. 14. Flowchart of the modified FPP method.

4.0 Experiment of the Modified Fringe Projection Methods

In the previous section, we focused on the physical principles behind the traditional FPP method, such as system geometric relationships, fringes analysis algorithms, system calibration mathematical models and unwrapping algorithms. In this chapter, we will focus on the application of the polarization FPP method on a real LPBF printing machine, including the details of the projector-camera system setup, the application of linear polarizers and the data analysis of the experimental results.

4.1 Modified FPP Method using fringe patterns with more phase steps

In order to compare the accuracy of 3-step phase shifting with 12-step phase shifting, we generated corresponding stripe patterns in MATLAB for projection respectively. Due to the uncontrollable aperture of the camera, a large amount of overexposure occurred in the experiment, so we improved the stripes to prevent them from being captured by the camera in the overexposed area by making their spacing length larger but less than 2 mm (to ensure that the resolution of the measurement would not receive a drastic impact), as shown in Figure 17.

The reasons why we choose 12-step phase shifting algorithm are listed as follow,

(1) Improved accuracy: A larger phase shift (3-step's $\pi/3$ which is larger than 12-step's $\pi/12$) can increase the likelihood of phase wrapping, which occurs when the phase shift exceeds 2π and wraps around to the beginning

(2) Better resolution: The smaller phase shift allows the software to capture more high-frequency information about the object's surface.

(3) More robustness to surface texture: The smaller phase shift captures more detail about the surface

(4) More flexibility: The smaller step phase shift allows for a wider range of object shapes and surface textures to be accurately scanned

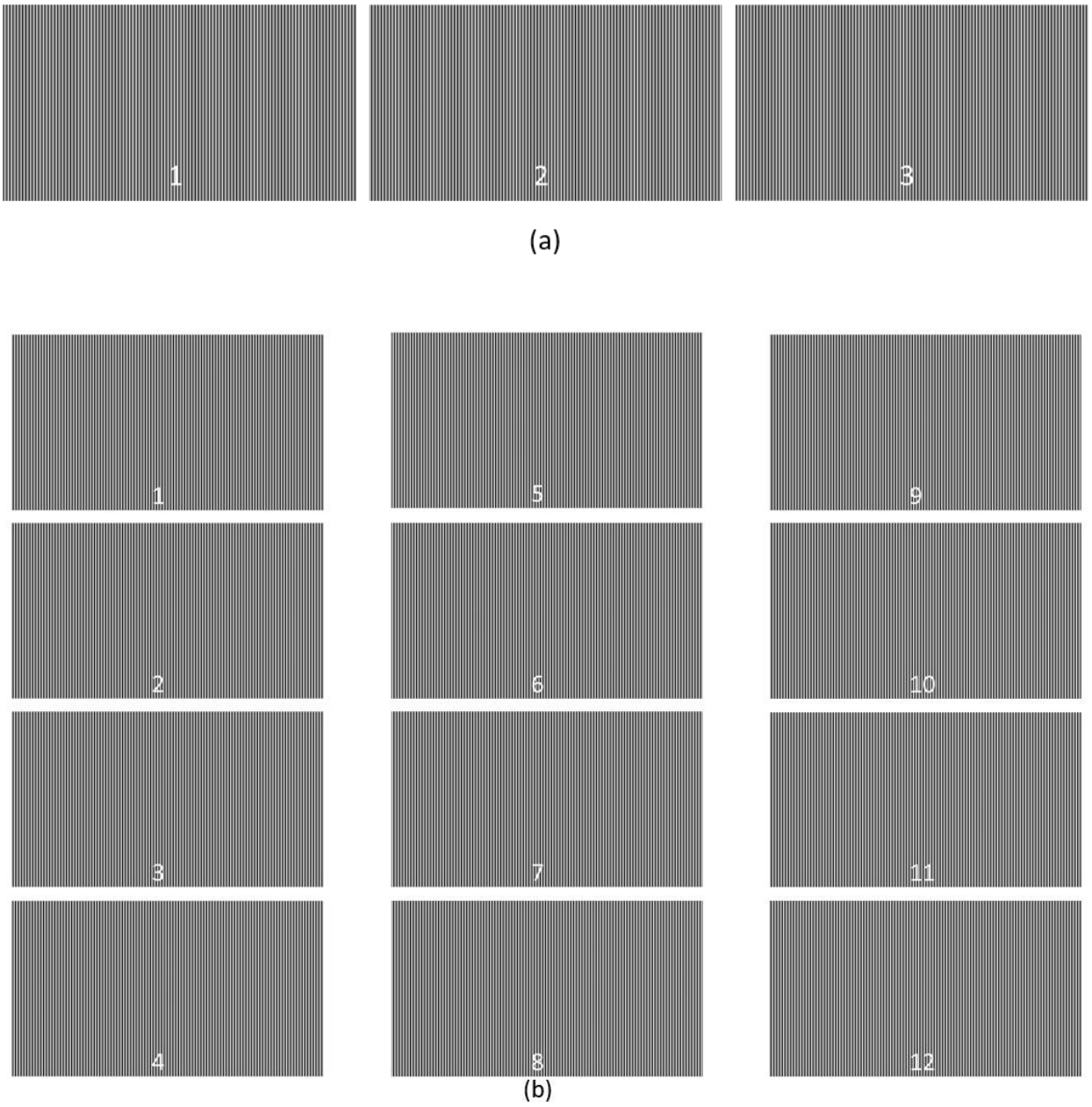

Fig. 15. (a) Projected 3 step phase shifting images. (b) Projected 12 step phase shifting images.

4.2 Modified FPP System Setup using Polarizer

Our FPP system is built on the two circular windows of the EOS M290 DMLS machine. The window projector projects the stripe pattern into the print chamber, and the camera captures the light pattern reflected from the measured surface through the windows. The EOS M290 has the broadest material portfolio and the most robust and well-developed system on the market currently, accompanied by a 400W fiber laser that brings excellent detail resolution to the finished print. A DLP projector (LightCrafter 4710 EVM G2, Texas Instruments, Dallas, TX) and CMOS camera (Blackfly S USB3 30 FPS Mono, Teledyne FLIR LLC, Wilsonville, OR) were selected as the imaging system. The structure of the system is as shown in Figure 15. Besides, in the figure, by the position of the camera and the projector, we can get the geometric schematic of the whole system and we can roughly determine the approximate range of $K(x, y)$ follow-up by it.

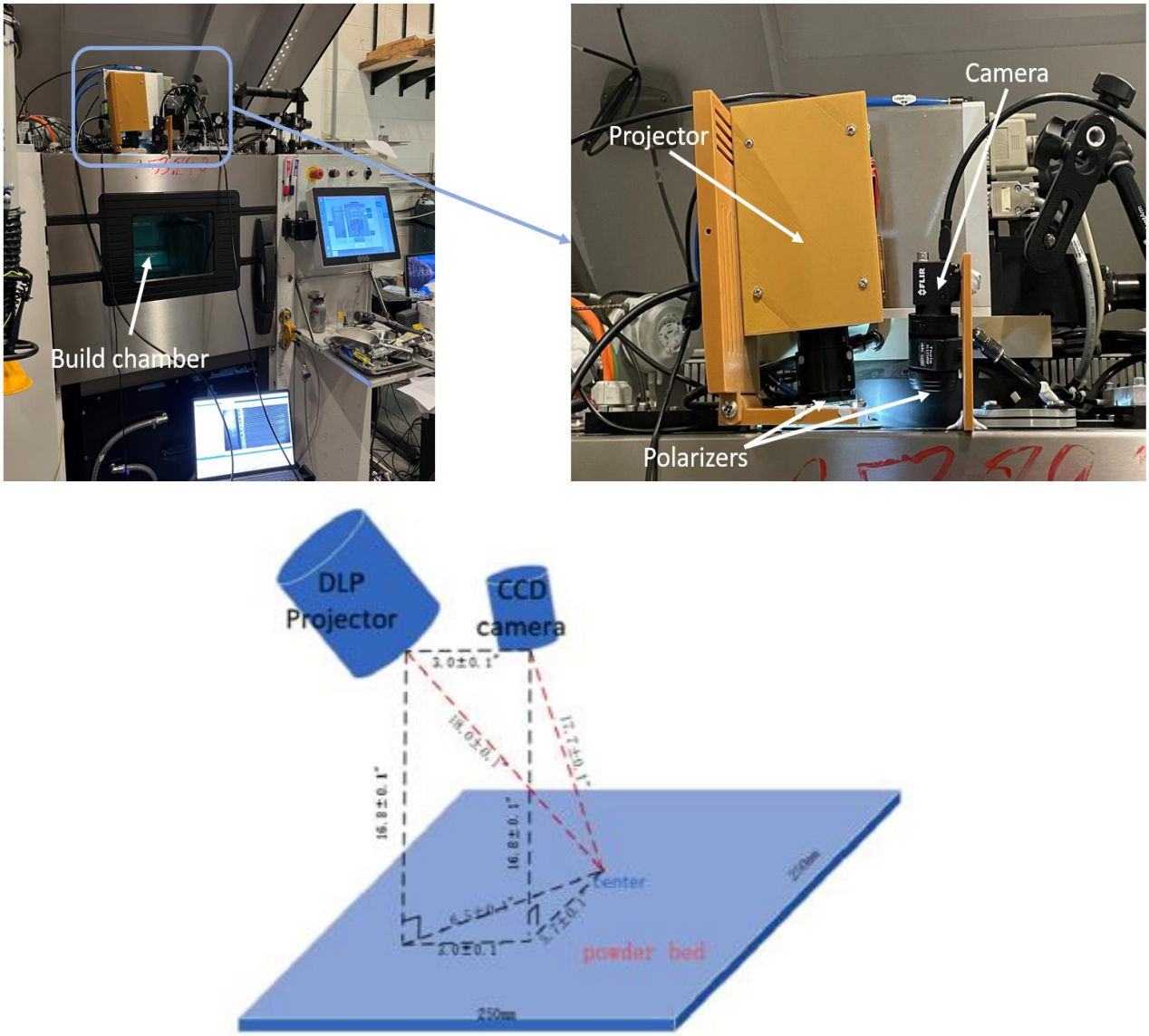

Fig. 16. (a) Schematic of the developed FPP system. (b) Geometrical diagram of the FPP system [Zhang H, Vallabh C K P, Xiong Y, et al. 2022].

In addition to using the conventional FFP system, since the light projected by the DLP projector is all visible light, we selected polarizers that filter the visible light range and therefore introduced an economical thin film polarizer (Dichroic Film Polarizer for Visible Light 400 - 700 nm, Thorlabs, Newton, NJ) to linearly polarize the light. Its specific parameters are shown in Figure 16.

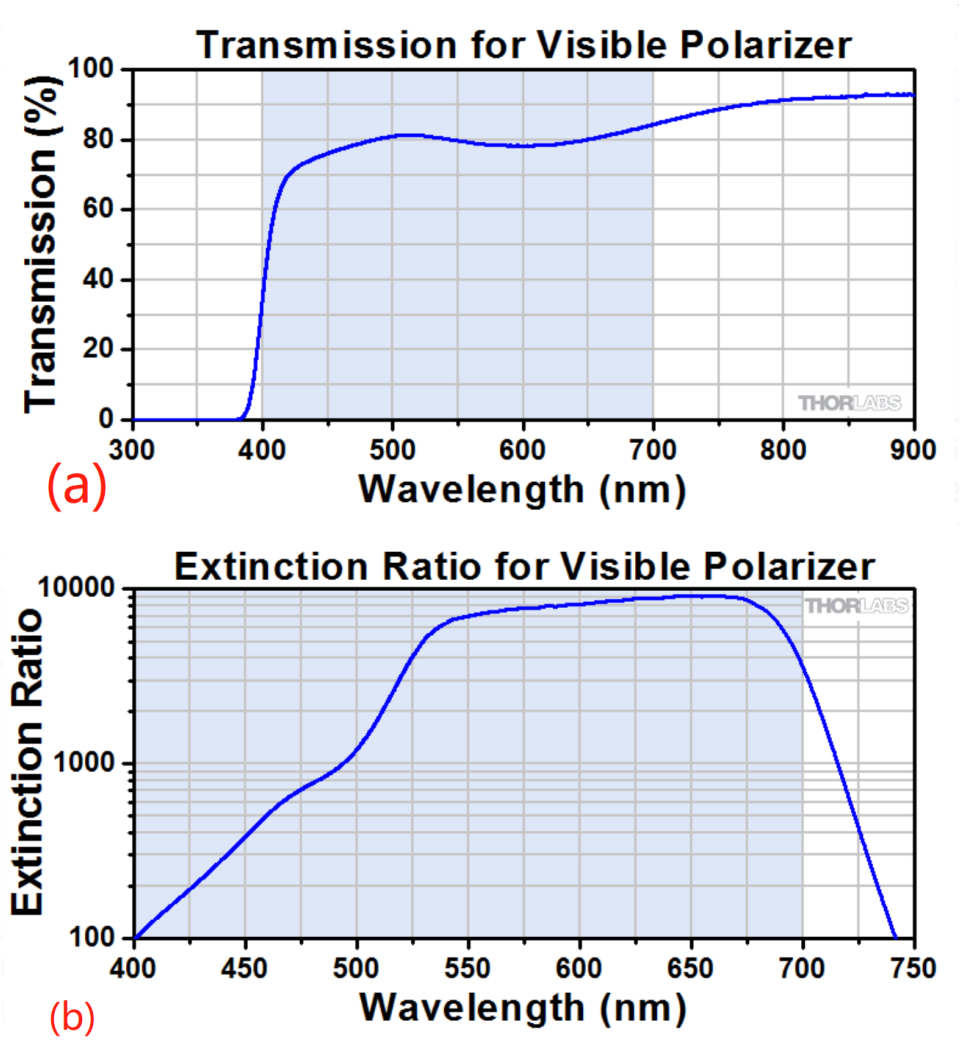

Fig. 17. (a) Transmission ratio for film polarizer. (b) Extinction ratio curve for polarizers [Thorlabs, 2012].

The shaded area in figure (a) indicates the spectral range in which we propose to use a polarizer; the shaded area in figure (b) indicates the spectral range in which we propose to use a polarizer. The extinction ratio (ER) is the ratio of the maximum transmission to the minimum transmission of a sufficiently linearly polarized input. The transmission reaches the maximum when the transmission axis is parallel to the input polarization; rotating the polarizer by 90°, the transmission reaches the minimum. In two experiments, we tested the angle between the two polarizers at 45° and 70°, and finally chose 45° as the angle setting by comparing the number and

proportion of overexposure points of the pictures, which is good and does not reduce the sharpness of the pictures too much.

4.3 Calibration Results

For the calibration of the camera and projector intensities (mentioned in Section 3.3.2), we performed the calibration by projecting 17 grayscale maps with different intensities (intensities of 15, 30, ... , 240, 255) to the measurement plate plane for the calibration calculation with and without polarizer respectively. After the corresponding calibration, we found that in the process without polarizer, the last grayscale image with intensity greater than 225 is prone to overexposure, so we chose to remove the three intensity images of 225, 240, and 255 from the calculation in C_{xy} calibration, as shown in Figure 18.

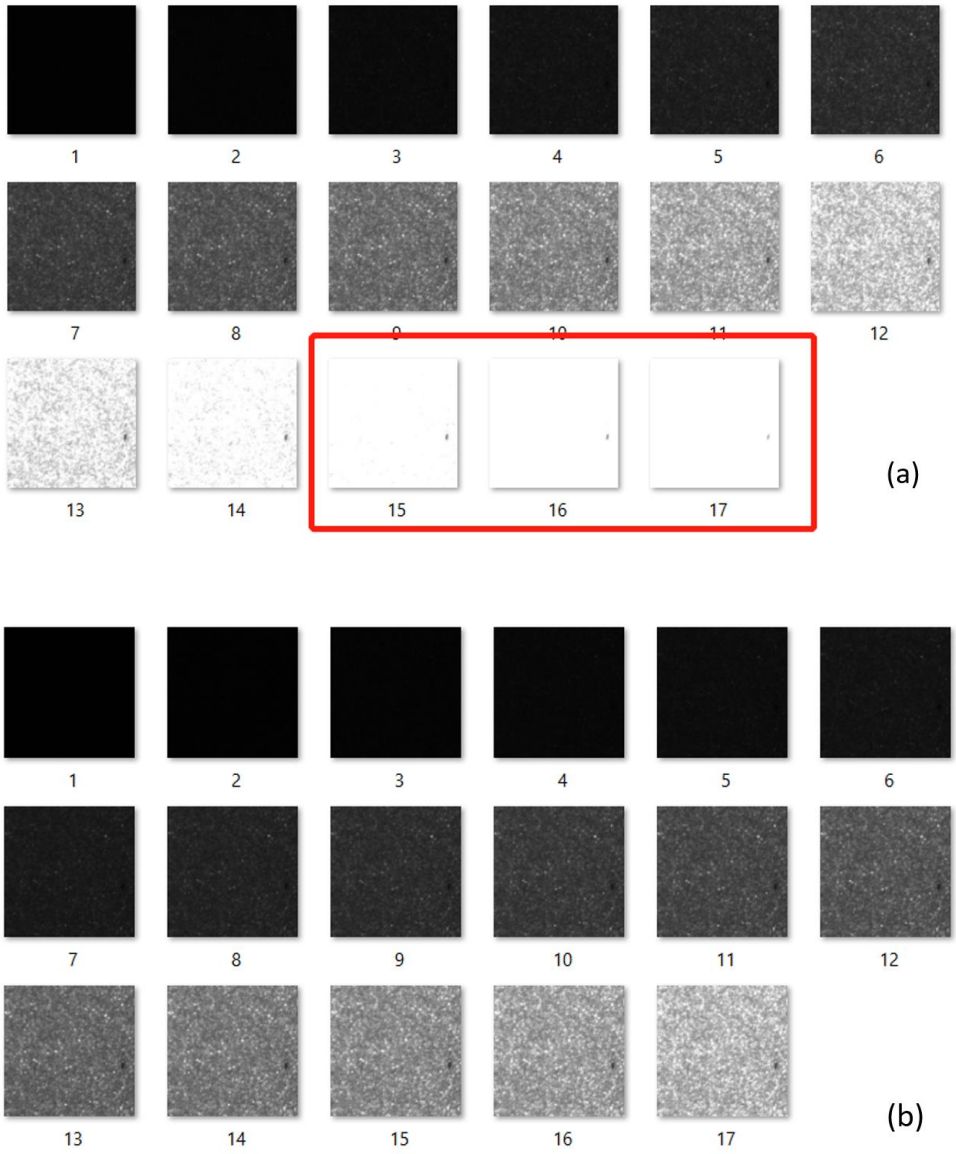

Fig. 18. The same intensity projection images captured by the camera: (a) without polarizers; (b) with polarizers.

We finally obtained the $\boldsymbol{C_{xy}}$ calibration curves (four vertices and the center point) with and without polarizers respectively, as shown in Figure 19. Each curve fits well and is suitable for the subsequent $K(x, y)$ calibration and FPP calculation.

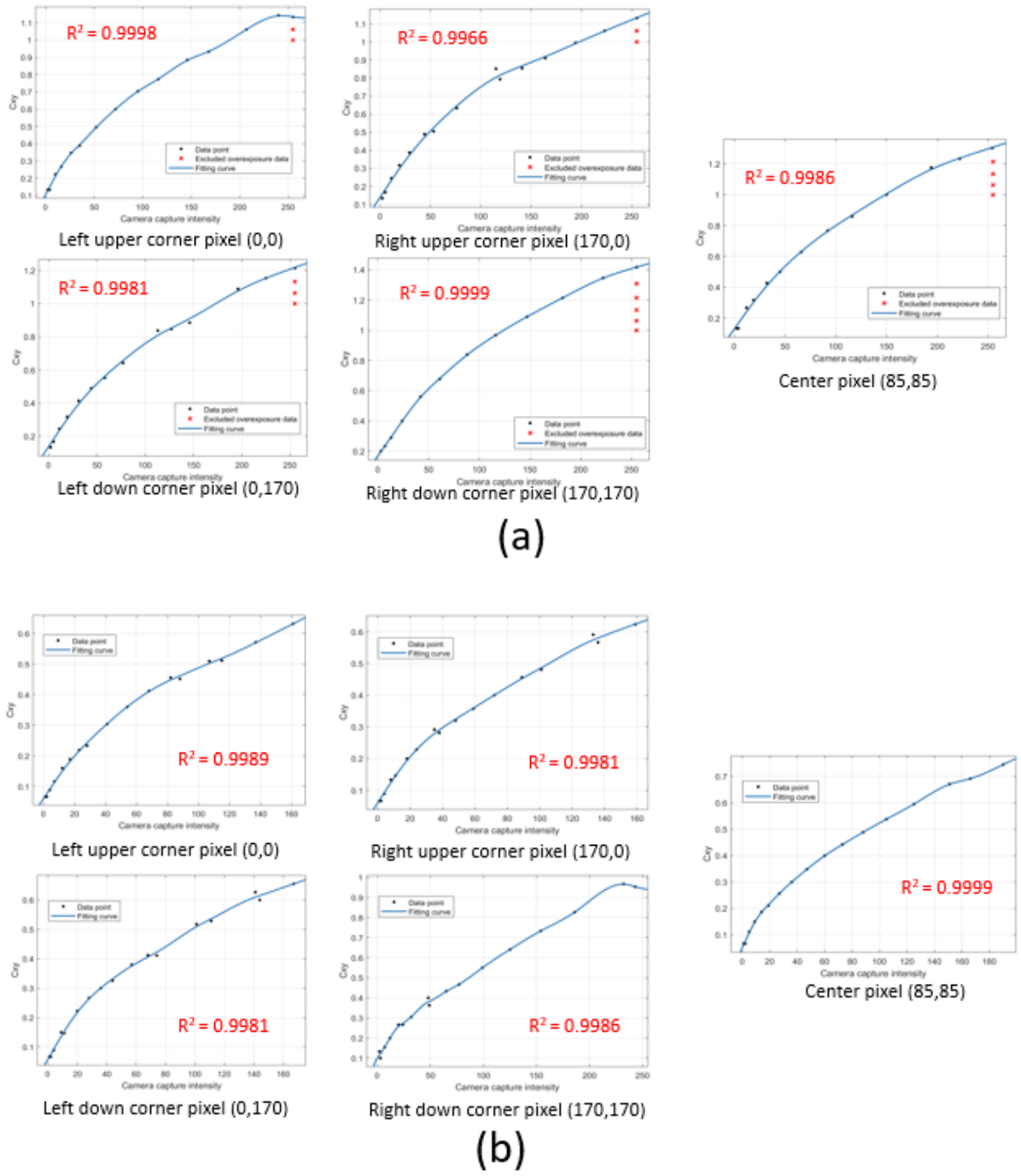

Fig. 19. C_{xy} **correction factor estimated by spline regression fitting at the center and four vertices. (a) without polarizers; (b) with polarizers.**

For the *K(x, y)* calibration mentioned in Section 3.3.1.1, since the height of the target print object is set at 40 μm, our experiment in this paper selects 10 μm as the calibration step size of Out-of-plane, i.e., we move the print platform 10 μm each time for a total of ten times, and the camera captures the 3 step phase shifting images after each move for unwrapping calculation to obtain pixel-wise unwrapped phase linear fit results. In the process of processing the data, we found that the spectral frequency sensitivity of the camera was larger than the moving step of the platform, which led to a 'jump error' in the phase unwrapping process of *K(x, y)*'s results. Therefore, we observed the *K(x, y)* results of the four vertices and intercepted the linear fit results of the same part of the trend as the final *K(x, y)* calibration results. The different *K(x, y)* calibration maps with and without polarizer and the *K(x, y)* fit curves for each vertex are shown in Figure 20 and Figure 21, respectively.

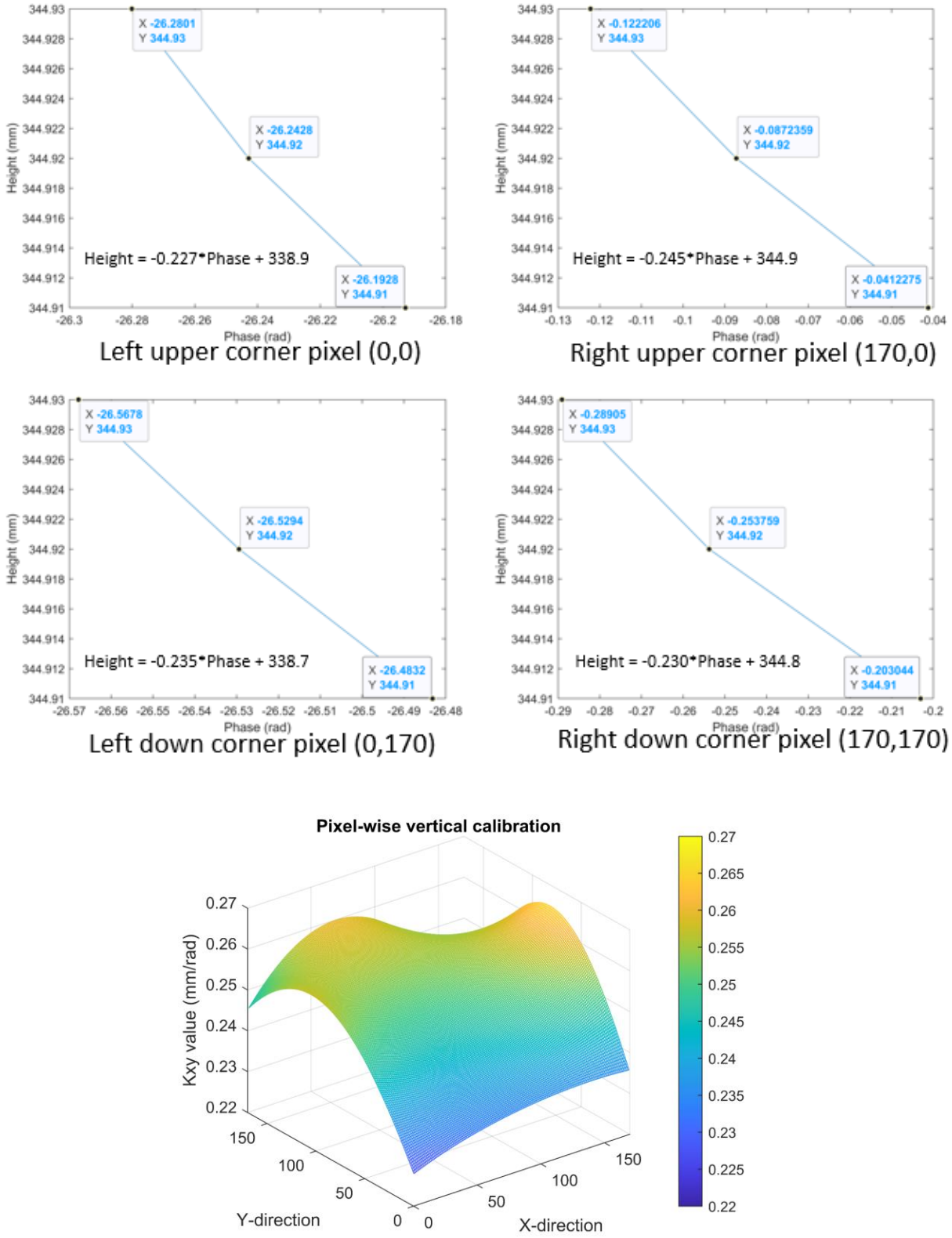

Fig. 20. Pixel-wise $K(x, y)$ calibration result without polarizers.

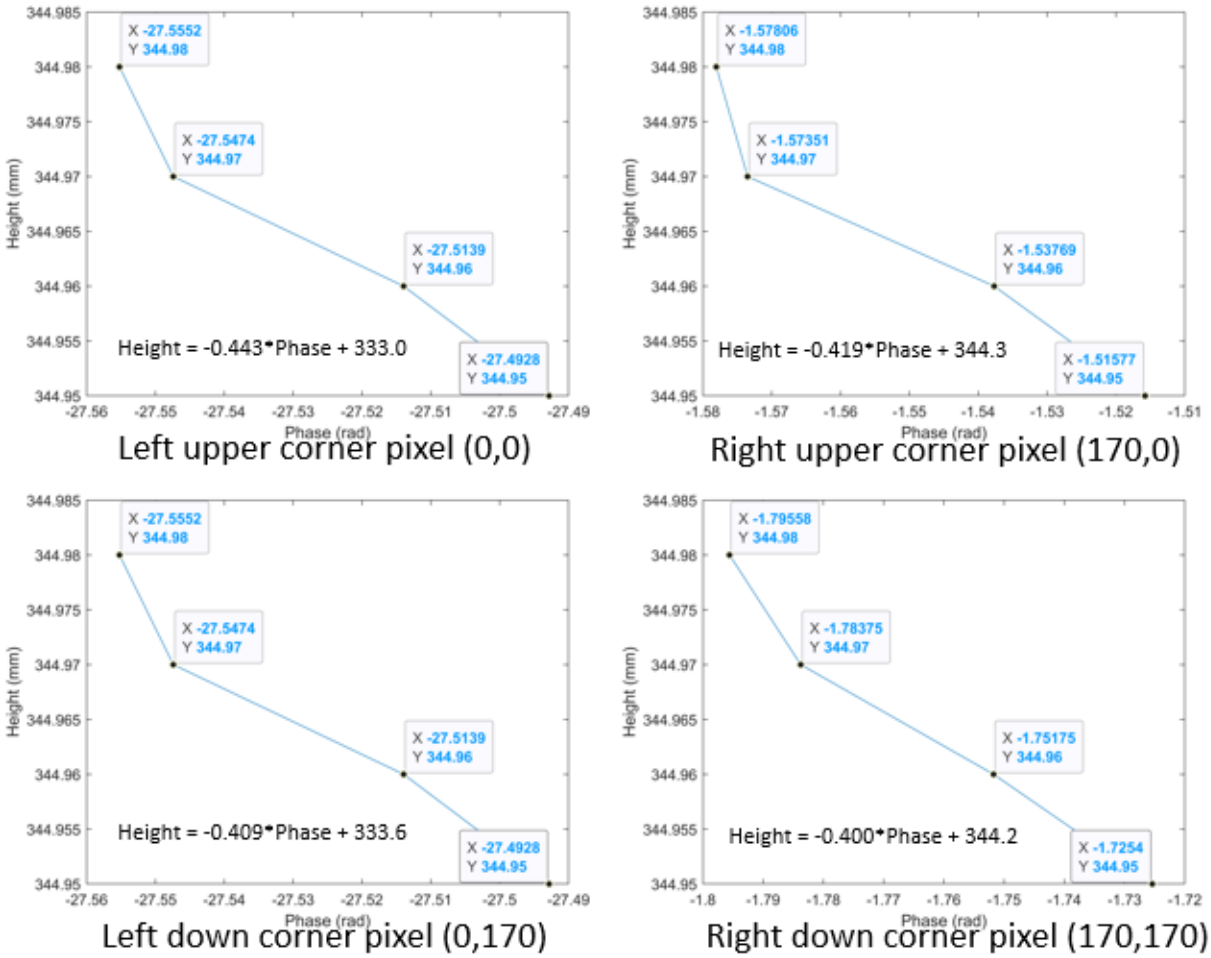

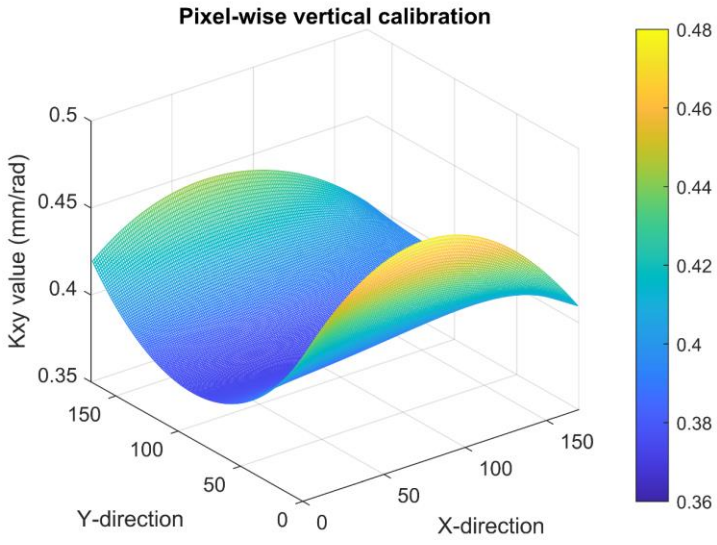

Fig. 21. Pixel-wise $K(x, y)$ calibration result with polarizers.

4.4 FPP Measurement Results

The measured objects used in the experiment were 39 single-layer square blocks (10 mm × 10 mm) printed on a 4 × 4-inch build plate, which was manufactured using an EOS M290 DMLS AM machine. The layer height of the square blocks was set to 40 μm, and the prevention of errors resulted in the printed sample on the right side being printed slightly outside the build plate. In the data analysis, the specific block in Figure 20 was selected as the focus area for measurement in order to be able to clearly compare the accuracy of the layer heights of the different methods. The Ex situ measurement of the print was also performed using an optical 3D profiler (Keyence VR3200, Keyence Corporationof America, IL, USA) with an ex-situ characterized HR profiler surface profile with a lateral resolution of ~5 μm, much larger than the lateral resolution output by the conventional FPP method (~40 μm).

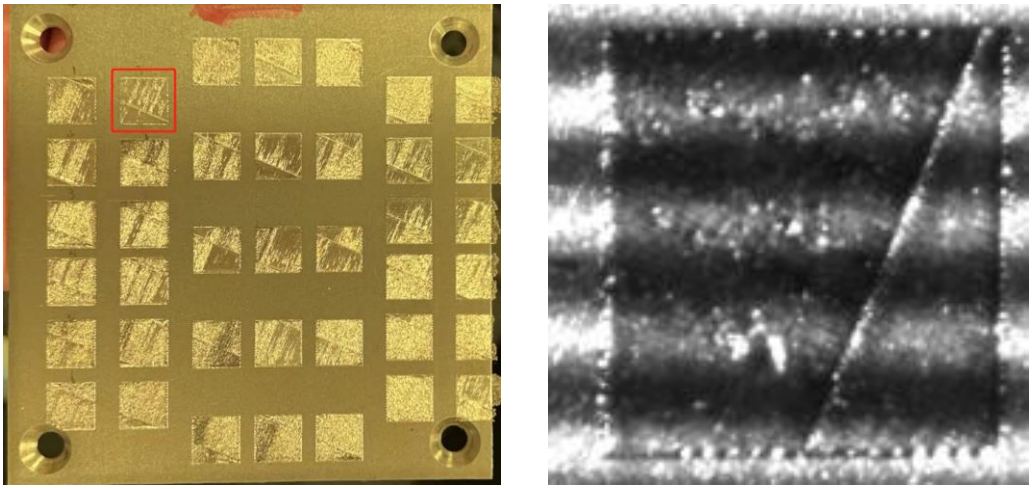

Fig. 22. Specific block selection in the whole printed plate (left one). Camera captured image with fringes of the selected block.

Due to the unquantifiable nature of the camera aperture, we compare the results of three sets of experiments by labeling the number of overexposure points in the camera capture pictures

to detect the effect of polarizer on the reduction of specular reflection. From the results, it can be obtained that the percentage of overexposure points in the grayscale map decreases (number of overexposure points/total number of pixel points) after adding polarizers in each group of experiments, and the fringe information is more complete, and the overexposure points in the three experiments with and without polarizers are marked in Figure 23 (blue marked points). The percentage of overexposure points decreases from 0.38% to 0.0033% in the first group of experiments, from 2.53% to 0.1% in the second group of experiments, and from 24.52% to 0.28% in the third group of experiments. Therefore, we conclude that the polarizer has a significant attenuating effect on the specular reflection on the smooth metal surface, and the subsequent data analysis is used to verify the effect of the polarizer on the accuracy of the FPP method.

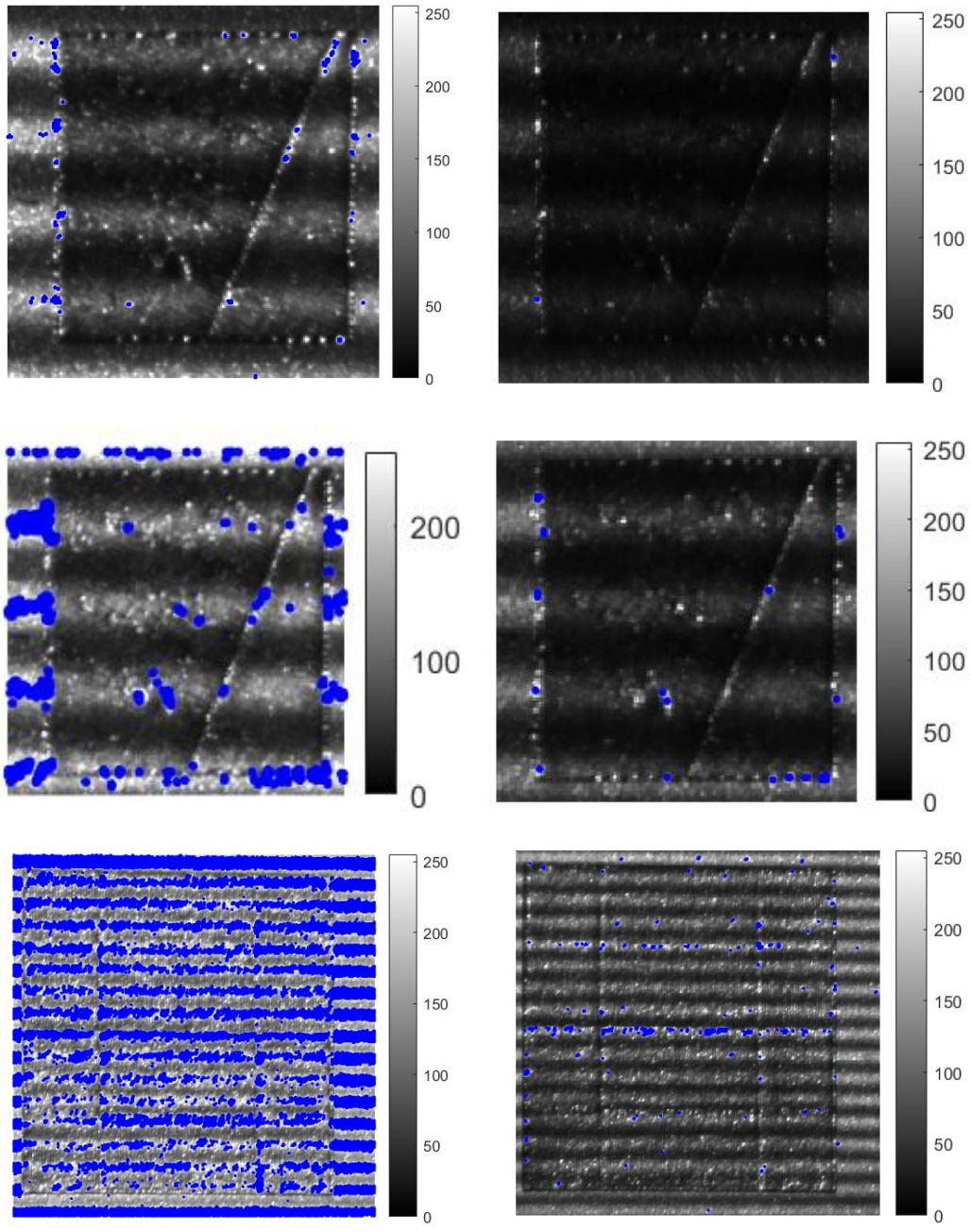

Fig. 23. Three sets of overexposure point labeling diagrams with and without polarizers.

Combining the calibration results in Section 4.2.1, we obtained the surface topography (with and without polarizers, respectively) for the corresponding 3 step phase shifting and 12 step phase shifting methods by FPP. As shown in Figure 24, comparing the morphology maps, we can observe that there is overexposure at the edges of the squares, at the edges of the camera capture

plane, and at specific formations (yellow bumps that are significantly larger in height than the average height). In the height map without polarizers, the overexposure phenomenon causes the height to change drastically due to the loss of information at that place, which is in error with the actual value. In the data with polarizer, the loss of information due to overexposure is reduced, but due to the characteristics of the polarizer, the signal-to-noise ratio decreases at the same time, and some of the detailed features are not clearly visible. By comparing the 3-step phase shifting method with the 12-step phase shifting method, it can be seen that the details of the image increase and at the same time reduce the drastic changes of some overexposure points. We will evaluate the accuracy of the different methods by comparing with Keyence results later.

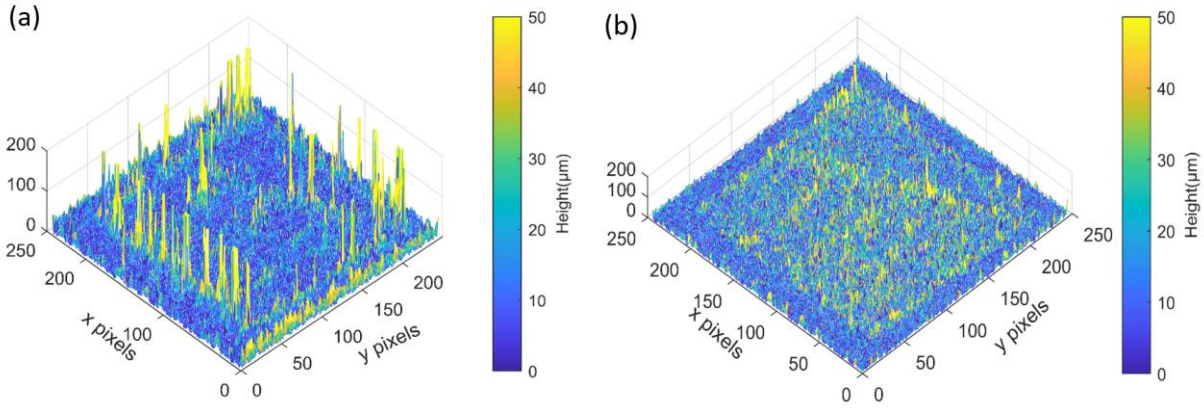

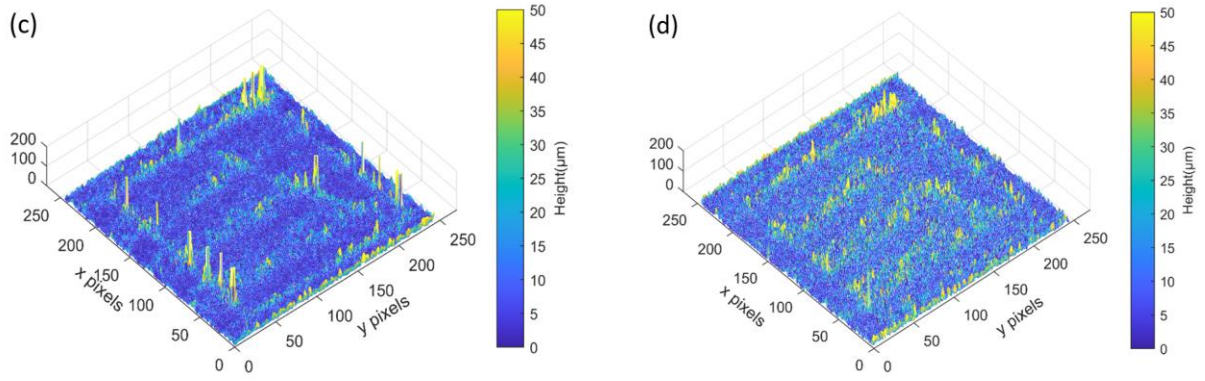

Fig. 24. FPP results in different experiment setup. (a) 3 step phase shifting without polarizers. (b) 3 step phase shifting with polarizers. (c) 12 step phase shifting without polarizers. (a) 12 step phase shifting with polarizers.

By comparing the image with the FPP height mesh results, we can find some special defects on the surface of the printed object that can be used as one of the criteria for judging the overall morphology, and we choose the block wrapped by the red border in Figure 25(a) as a demonstration. There is a more obvious pit defect in the red block. We compare the FPP results (Figure 25(b)(c)(d)(e)) with the camera captured image and find that the defect is clearly observed in the FPP mesh map without the polarizers, but the visibility of the defect is reduced in the mesh map with the polarizer attached. This is also one negative effect of the reduced signal-to-noise ratio as mentioned in the previous section.

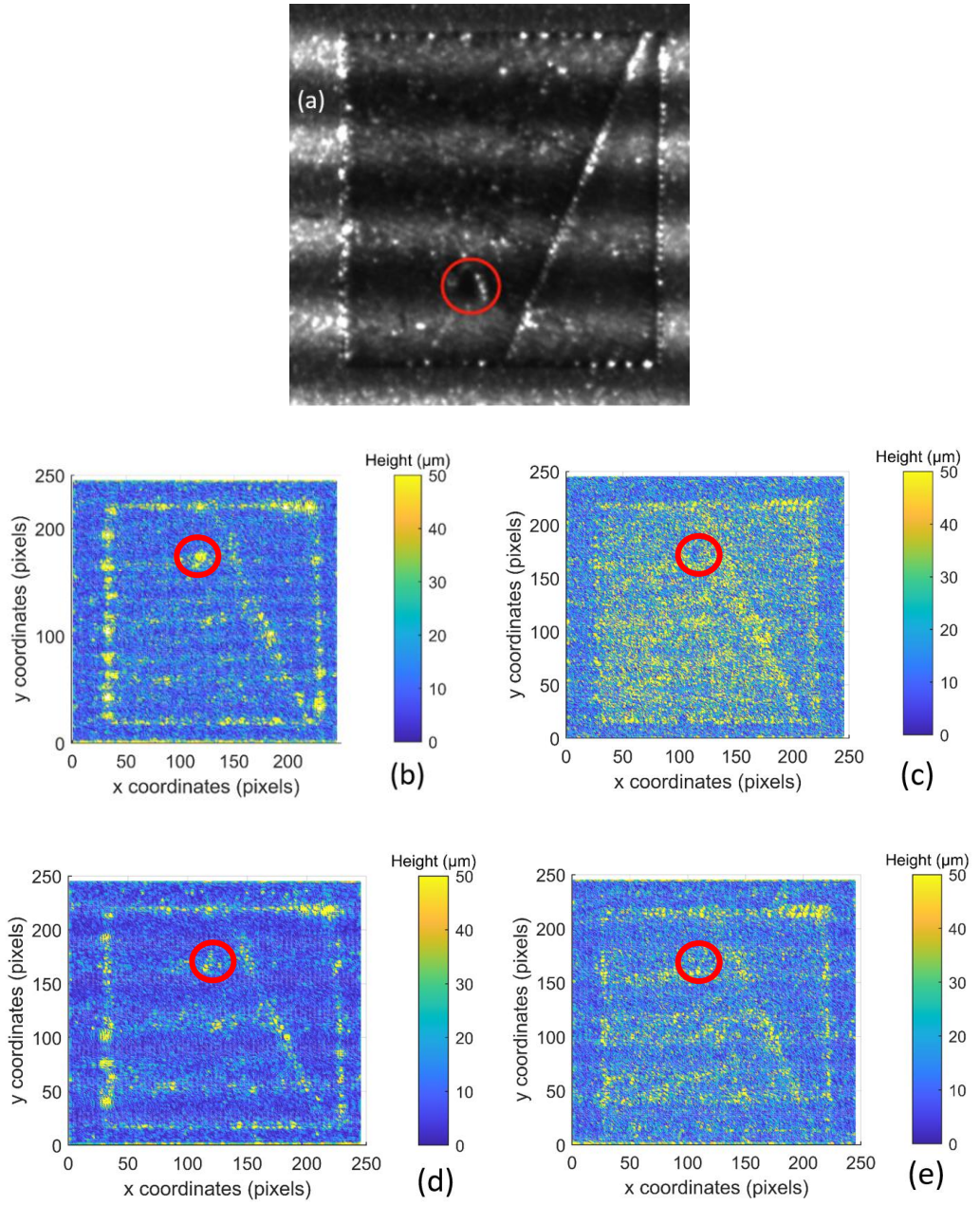

Fig. 25. Crater defects detected by FPP. (a) Camera captured imageCalculated height profile using: (b) 3-step phase shifting without polarizers; (c) 3-step phase shifting with polarizers; (d) 12-step phase shifting without polarizers; and (e) 12-step phase shifting with polarizers.

4.5 Validation of the Proposed FPP methods

In Section 4.2 we completed the corresponding calibration process and FPP measurement and morphology analysis and demonstrated that by combining polarizers will reduce the image overexposure rate and increase the information collection rate, but it may also bring a decrease in signal-to-noise ratio at the same time. Therefore, we would like to introduce an ex-situ height measurement method to verify the height measurement capability and height measurement resolution of our FPP method. Therefore, after completing a series of FPP method calculations, we compared the obtained height maps with the ex-situ measurements from a Keyence 3D profiler/microscope (Keyence VR3200, Keyence Corporation of America, IL, USA) to verify that the surface topographic features are credible, the Keyence height map shown in Fig. 25.. Since the extraction of information on the surface topography of printed objects by Keyence instruments is limited to linear contours and surface maps, we qualitatively verified the height of the printed square area and the linear contours corresponding to the surface topography.

First, we compared the height averages of the four FPP methods with the Keyence microscope results. The height average of the Keyence results was 12.7 μm, while the height average of the 3-step phase shifting (without polarizer) was 17.8 μm, leading to an error of 40.2%, mainly due to the height difference of the overexposed area. The height average of the 3-step phase shifting (with polarizer) was 13.7 μm and with an error of 7.8%. The average height of 12-step phase shifting (without polarizer) is 14.8 μm with an error of 8.6%. The average height of 12-step phase shifting (with polarizer) is 12.48 μm and with an error of 1.7%. Secondly, we also compare the surface roughness from these methods: Keyence measured *Ra* is 15.59; 3 step phase shifting measured *Ra* without polarizer is 18.39 with an error of 17.9%; 3 step phase shifting measured *Ra* with polarizer is 17.25 with an error of 10.6%; 12 step phase shifting measured *Ra*

withOUT polarizer is 12.91 with an error of 17.1%; 12 step phase shifting measured *Ra* with polarizer is 17.4 with an error of 11.6%.The above analyses on average height and roughness are detailed in Table 1. Note that the surface roughness measurement using FPP is calculated by Equation (20).

$$Ra = \sum_{i=1}^{N} \frac{\left(H_{pixel} - H_{average}\right)}{N} \qquad (4-1)$$

Where N is the number of pixels on the line profile selection, H_{pixel} is the height value in each pixels and the $H_{average}$ is the average height value of the line profile selection.

Table 1 Average Height and Ra for each method

	Keyence	3-step	3-step with polarizers	12-step	12-step with polarizer
Average Height	12.7 μm	17.8 μm	13.7 μm	14.8 μm	12.48 μm
Height Error	N/A	40.2%	7.8%	8.6%	1.7%
Ra	15.59 μm	18.39 μm	17.25 μm	12.9 μm	17.4 μm
Ra Error	N/A	17.9%	10.6%	17.1%	11.6%

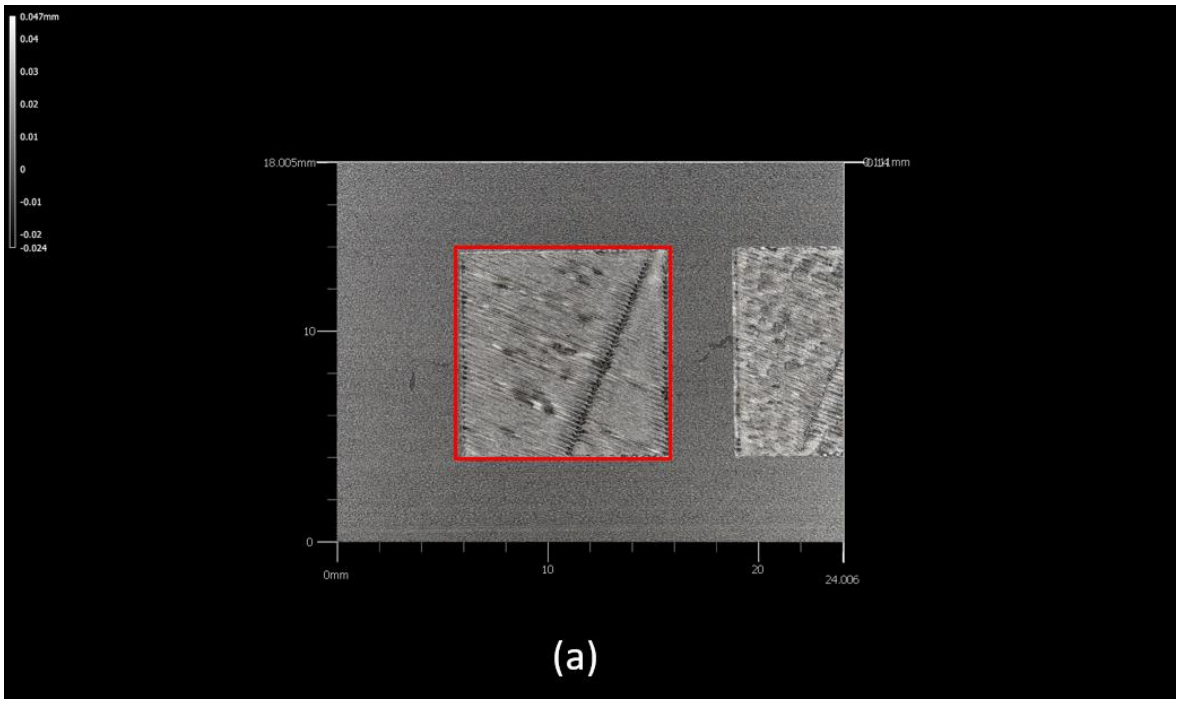
0.047mm
0.04
0.03
0.02
0.01
0
-0.01
-0.02
-0.024
18.005mm
10
0
0mm
10
20
24.006
(a)

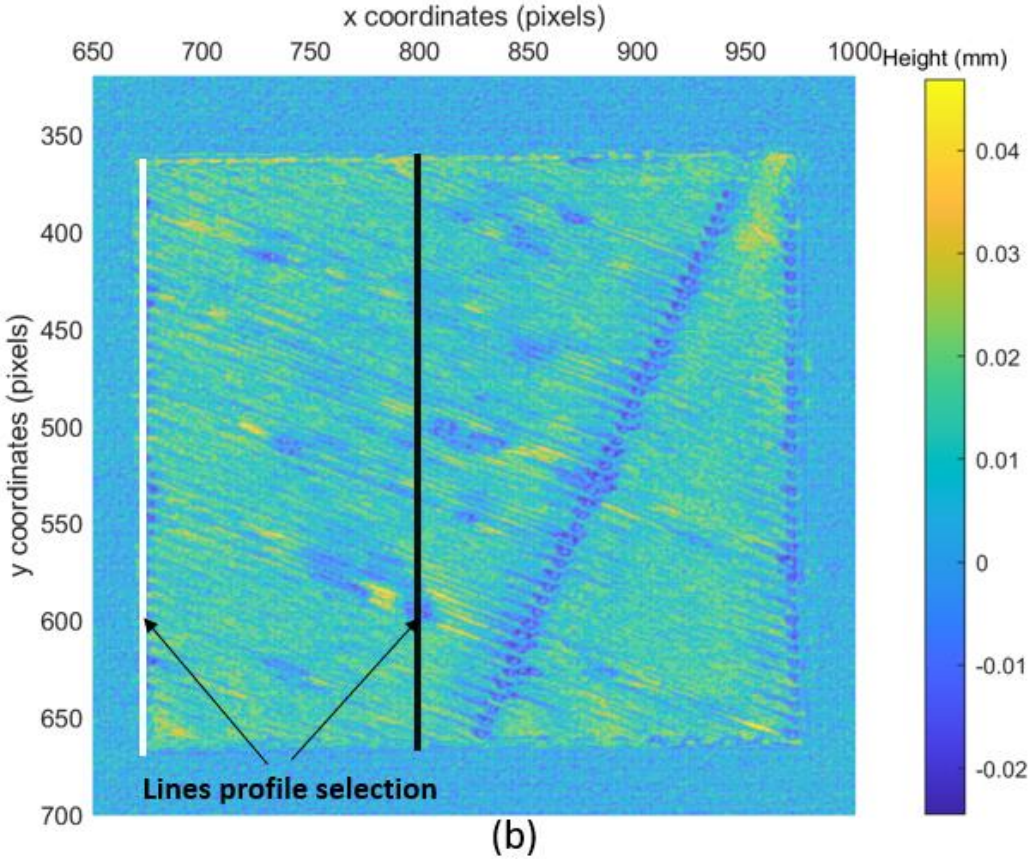
x coordinates (pixels)
650
700
750
800
850
900
950
1000
Height (mm)
0.04
0.03
0.02
0.01
0
-0.01
-0.02
y coordinates (pixels)
350
400
450
500
550
600
650
700
Lines profile selection
(b)

Fig. 26. (a) Keyence microscope result: grayscale height map. (b) Our FPP measurement result for the sample inside the red box in (a), plotted in mesh map in MATLAB. The white and black lines are the two selected line profiles measured in Keyence measurement.

To further characterize and verify the detailed contour gap, we compared the line contours at different locations of a specific surface morphology in the same print block. Two line contours were extracted from the location at the crater and the location at the left edge of the figure to compare the contour similarity between FPP and Keyence, as shown in Figure 25 (b) (the line contour at the pit location is a black straight line, and the line contour at the left border location is a white straight line). In Figure 26, (a)(b)(c)(d) compare the line height comparison between the FPP method and Keyence microscopy results for different step lengths and polarizer configurations at the left border of the print square, respectively. In the FPP method without polarizer (Fig. 26(a)(c)), there is a situation where some areas are overexposed and information is lost to obtain the correct height, which can be too low or too high, as shown in the height curve comparison in the green border box in the figure. In the FPP experimental results of the device polarizer, we can find that the polarizer smoothed out the whole line profile, and the height feature as a whole is at a horizontal value (i.e., at 20 μm), which indicates that the polarizer filters out the high overexposure area (i.e., the result of the comparison of the number of overexposure points in Figure 23) while filtering other surface morphological details at the same time, which will have a certain impact on the accuracy of defect monitoring.

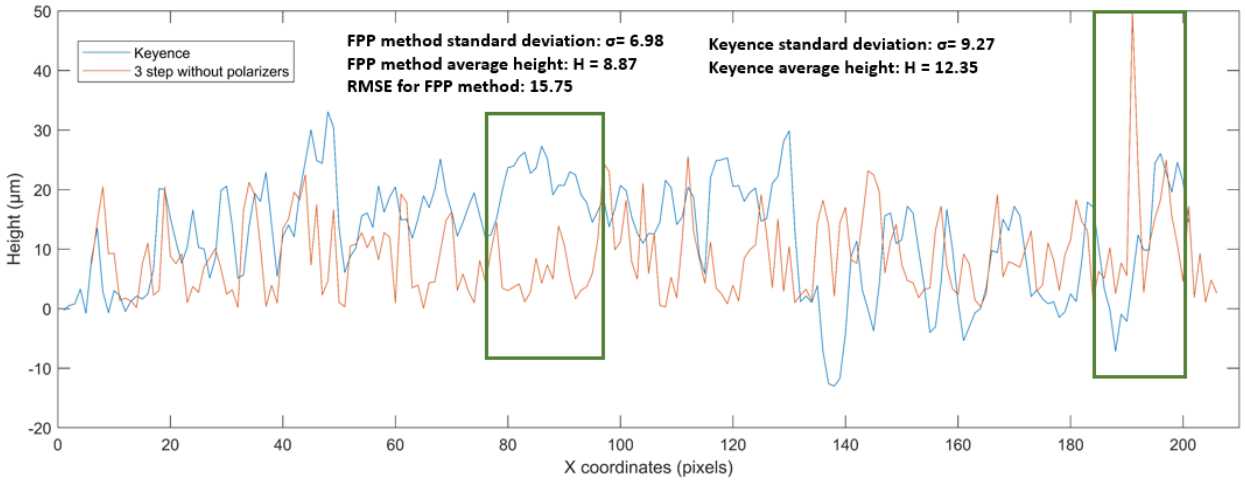
Keyence
3 step without polarizers
FPP method standard deviation: σ= 6.98
FPP method average height: H = 8.87
RMSE for FPP method: 15.75
Keyence standard deviation: σ= 9.27
Keyence average height: H = 12.35
Height (µm)
X coordinates (pixels)

(a)

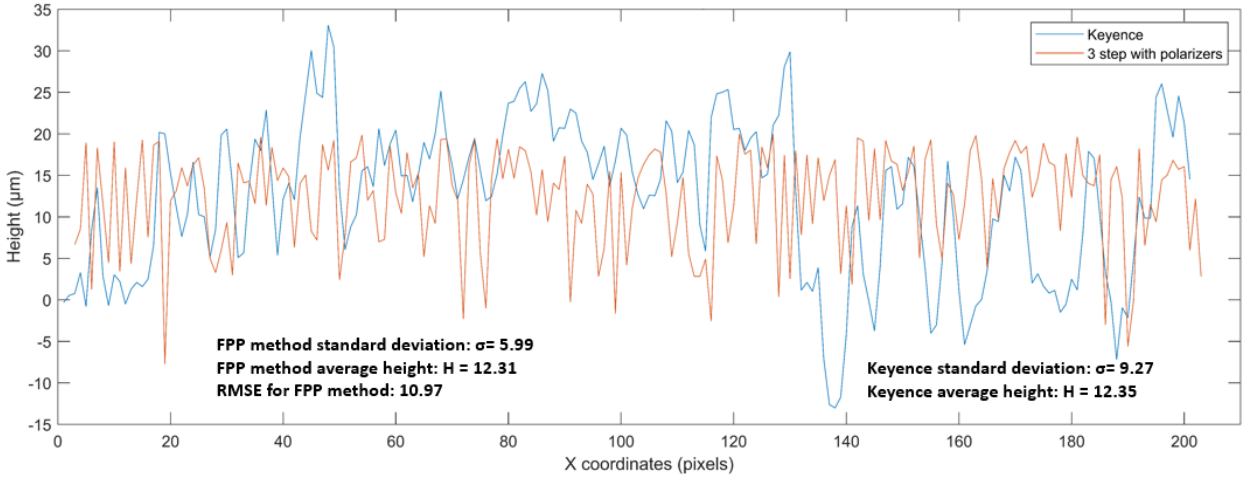
Keyence
3 step with polarizers
FPP method standard deviation: σ= 5.99
FPP method average height: H = 12.31
RMSE for FPP method: 10.97
Keyence standard deviation: σ= 9.27
Keyence average height: H = 12.35
Height (µm)
X coordinates (pixels)

(b)

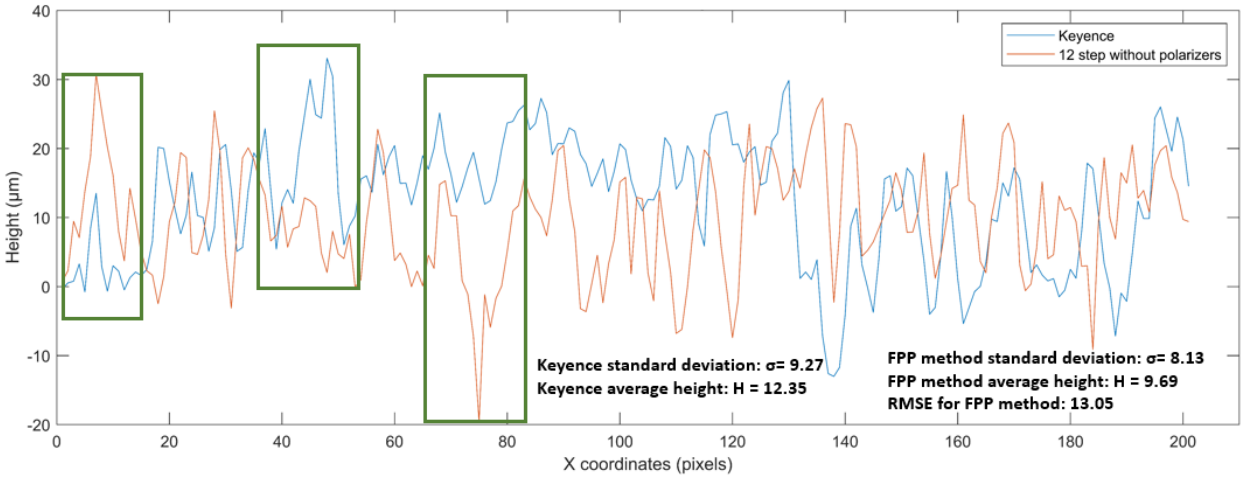
Keyence
12 step without polarizers
Keyence standard deviation: σ= 9.27
Keyence average height: H = 12.35
FPP method standard deviation: σ= 8.13
FPP method average height: H = 9.69
RMSE for FPP method: 13.05
Height (µm)
X coordinates (pixels)

(c)

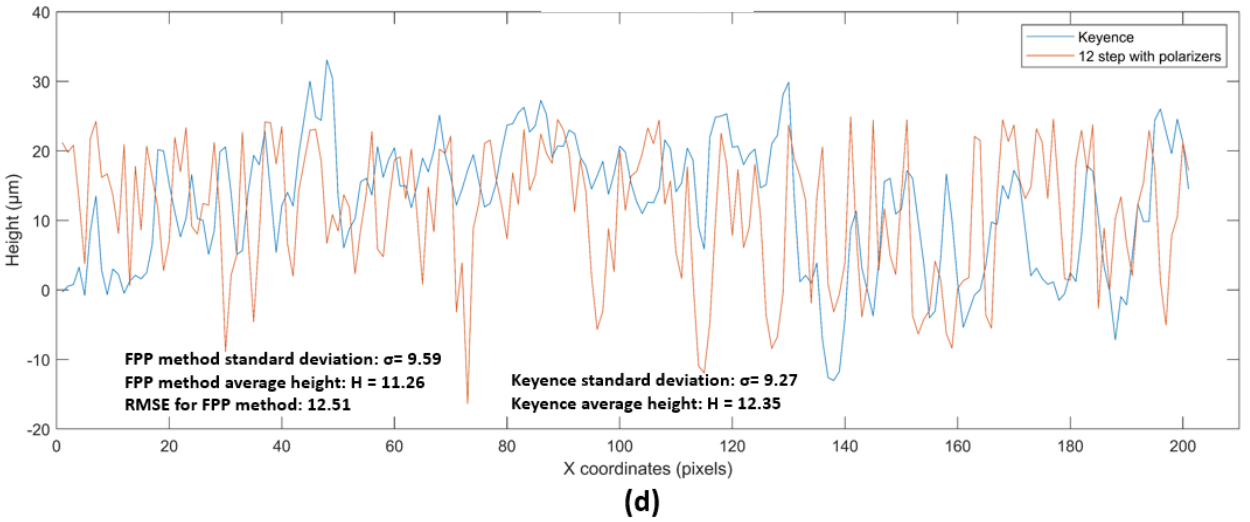

(d)

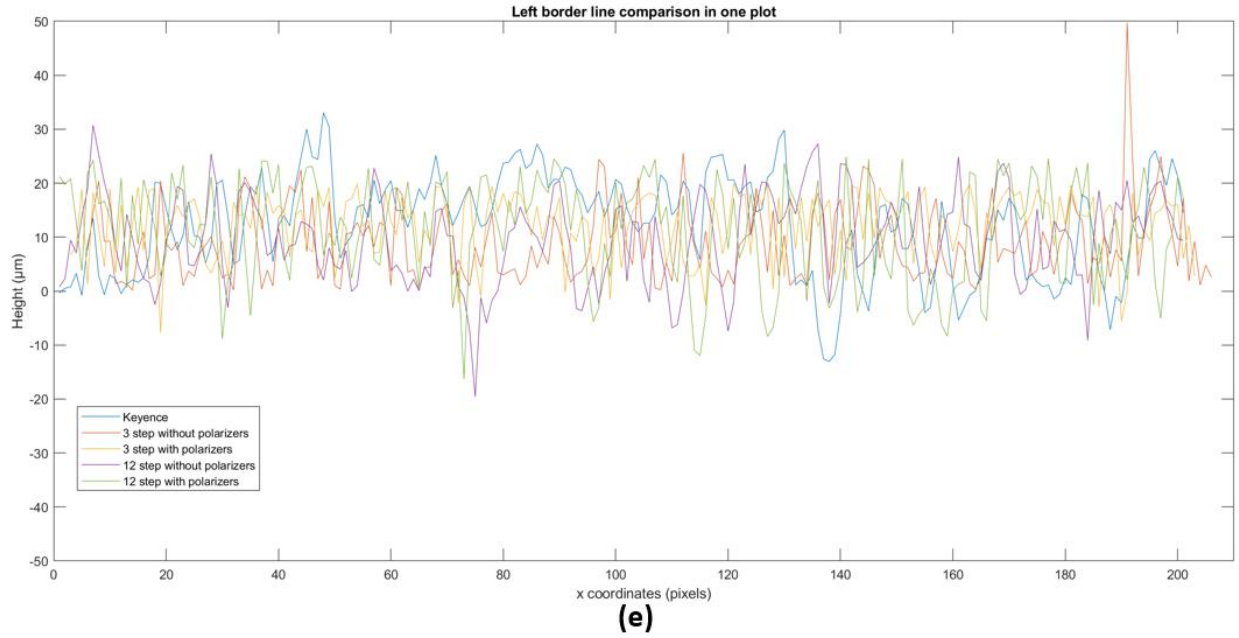

(e)

Fig. 27. Left border line profilemeasured by FPP vs. by Keyence. (a) 3 step phase shifting without polarizers. (b) 3 step phase shifting with polarizers. (c) 12 step phase shifting without polarizers. (d) 12 step phase shifting with polarizers. (e) All methods.

Similarly, comparing the line profile intercepted at the location of the crater with the Keyence microscopy results, we can find the defect of the crater (diameter size ~1 mm) in each FPP method. Comparing the results of the experimental groups with and without polarizers, we

can find that the results of the FPP experimental group with polarizers are closer to the Keyence results, while the results of the experimental group without polarizers in 3 steps have overexposure at the depth of the pits affecting the specific values (as shown in Figure 25 (a)). At the same time, due to the intervention of the polarizer, the rest of the shape of the two groups of data is smoothed out, which cannot reflect the height shape of the rest of the linear contour, as shown in Figure 27, which is similar to the result of the left border of the printed square. Therefore, we tentatively judge that the polarizer will filter the morphological features smaller than a specific value in the FPP measurement. This indicates that the polarizer has some limitations in monitoring defects in the traditional FPP method.

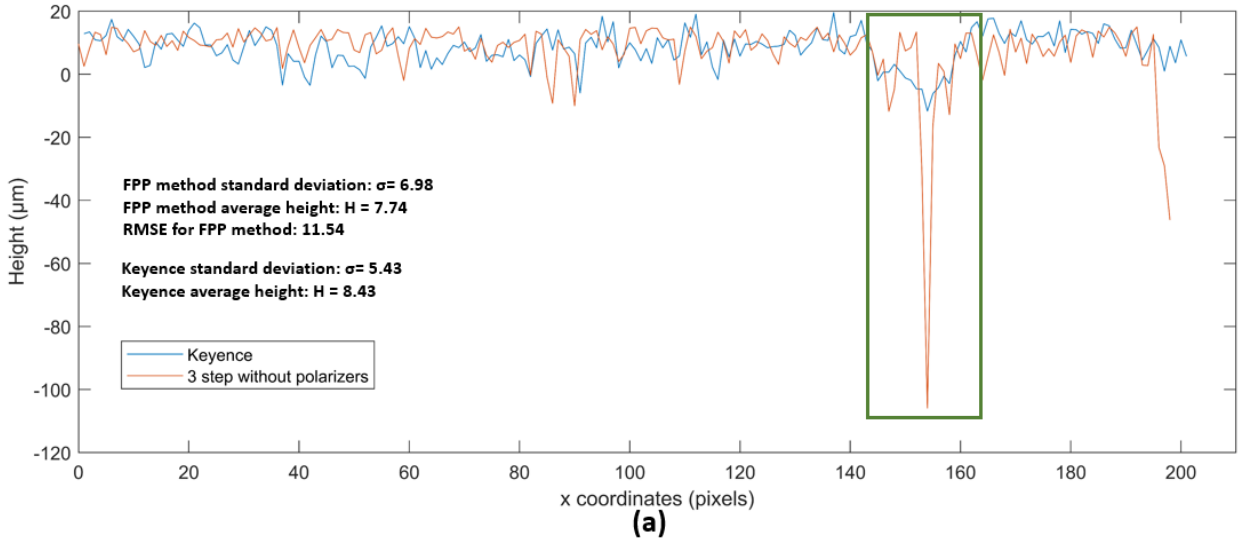

(a)

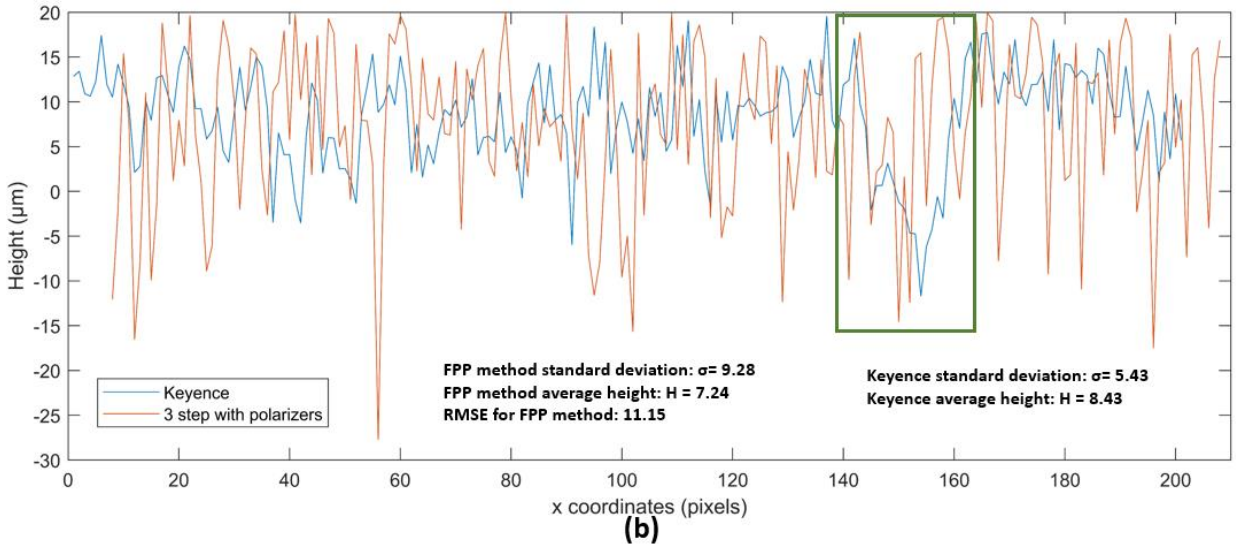
Height (μm)
x coordinates (pixels)
Keyence
3 step with polarizers
FPP method standard deviation: σ= 9.28
FPP method average height: H = 7.24
RMSE for FPP method: 11.15
Keyence standard deviation: σ= 5.43
Keyence average height: H = 8.43

(b)

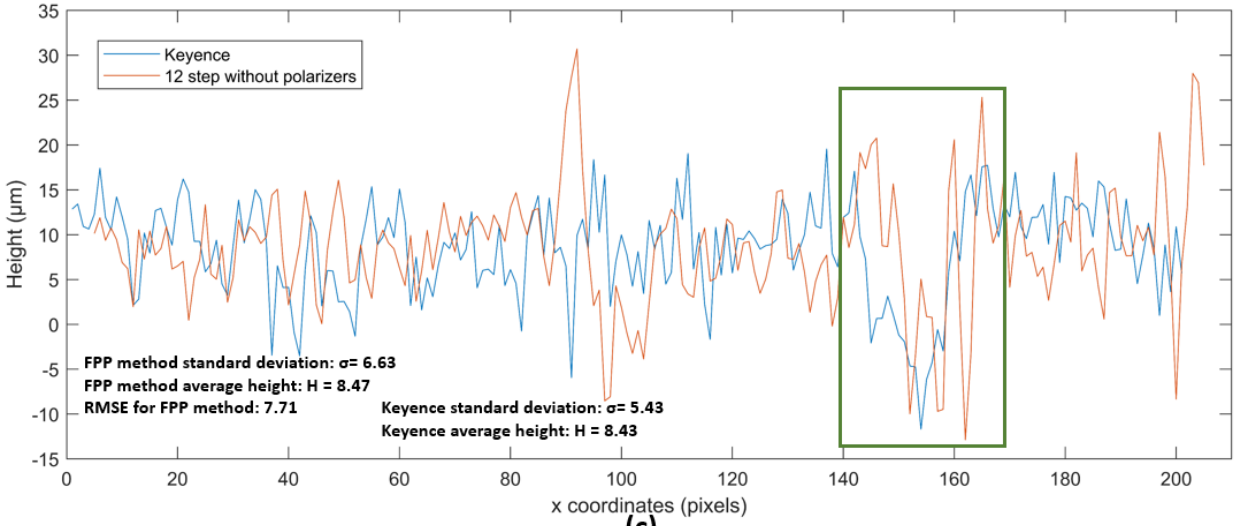
Height (μm)
x coordinates (pixels)
Keyence
12 step without polarizers
FPP method standard deviation: σ= 6.63
FPP method average height: H = 8.47
RMSE for FPP method: 7.71
Keyence standard deviation: σ= 5.43
Keyence average height: H = 8.43

(c)

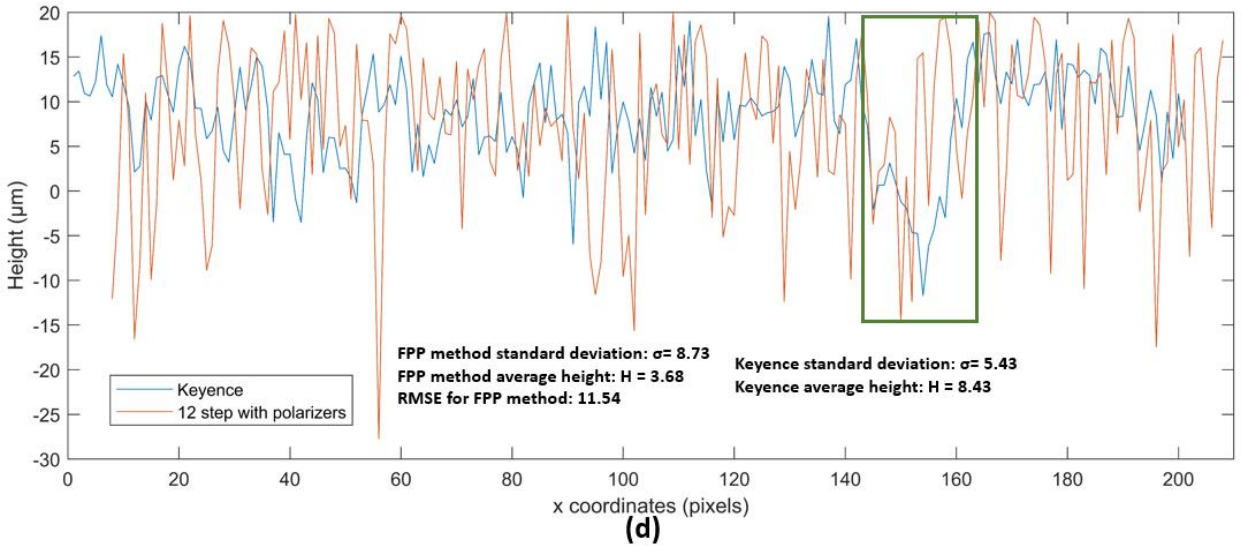

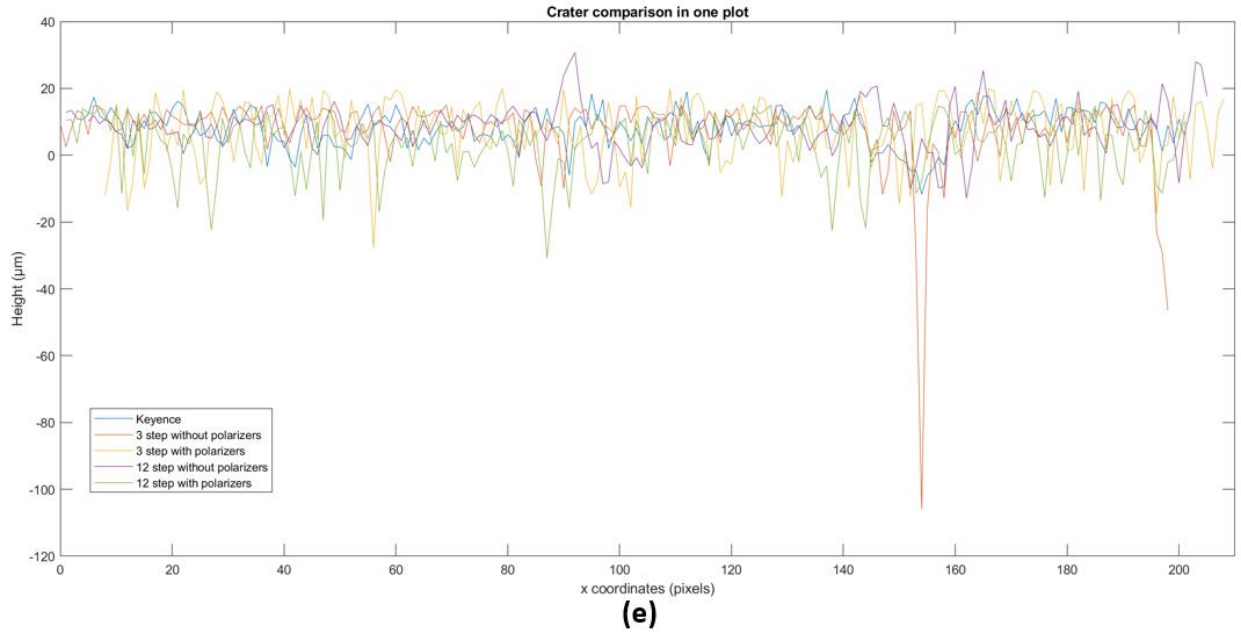

Fig. 28. Crater line's FPP height result comparison with Keyence. (a) 3 step phase shifting without polarizers. (b) 3 step phase shifting with polarizers. (c) 12 step phase shifting without polarizers. (d) 12 step phase shifting with polarizers. (e) All methods.

Table 2 compares the FPP and Keyence microscope performance in the two sample lines' profile measurements using average height, standard deviation and surface roughness as metrics.

Table 2 Evaluate the Performance of proposed FPP Methods by Comparing the Sample Lines' and Whole Block's Profile Measurement Results - Average Height and Standard Deviation

		Keyence	3-step	3-step with polarizers	12-step	12-step with polarizer
Crater	Average Height (μm)	12.35	8.87 (28.2% error)	12.31 (0.3% error)	9.69 (21.5% error)	11.26 (8.8% error)
	RMSE (μm)	N/A	11.54	11.15	7.71	10.96
	Ra (μm)	5.41	11.26 (108.2% error)	9.26 (71.2% error)	8.71 (60.9% error)	6.61 (22.2% error)
Left border	Average Height (μm)	8.43	7.74 (8.2% error)	7.24 (14.1% error)	8.47 (0.5% error)	3.68 (56.3% error)
	RMSE (μm)	N/A	15.75	10.97	13.05	12.51
	Ra (μm)	9.25	5.97 (35.4% error)	6.96 (24.7% error)	8.11 (12.3% error)	9.56 (3.3% error)
Whole block	Average Height (μm)	12.7	17.8 (40.2% error)	13.7 (7.8% error)	14.8 (8.6% error)	12.48 (1.7% error)
	RMSE (μm)	N/A	13.25	11.27	10.82	9.97
	Ra (μm)	15.59	18.39 (17.9% error)	17.25 (10.6% error)	12.9 (17.1% error)	17.4 (11.6% error)

At the same time, we judge the improved method by comparing the curve similarity between different experimental groups and Keyence results, and the RMSE (the calculation equation is shown in the Equation (21)) is calculated for the linear shape of each FPP result with the surface shape of the above two linear profiles, respectively. We can see that the RMSE values

of the 12-step method are smaller in both the pit curve and the left boundary curve, and the overall results are closer to those of Keyence, which also verifies that increasing the step phase can improve the accuracy of the traditional FPP method. Meanwhile, in the comparison results with and without the addition of the polarizer, the RMSE values of the three groups are lower for the experiments with the polarizer, indicating that the height is close to the actual value, but the shape with smaller values cannot be fully observed due to the filtering of the polarizer.

$$\mathrm{RMSE} = \left[\sum_{i=1}^{N} \frac{\left(H_{fpp} - H_{keyence}\right)^2}{N}\right]^{\frac{1}{2}} \qquad (4-2)$$

Where N is the number of pixels in the height map, H_{fpp} is the height value of each pixel in FPP method result and the $H_{keyence}$ is the height value of the Keyence microscope measurement result.

5.0 Measurement Error Analysis

In the previous chapters, we went through the experimental process of calibrating projector-camera intensity and phase-change-to-height conversion , fringe projection using different phase steps and with/without polarizers, and validation by comparing against ex-situ microscopy. However, errors can be observed in the topography of the experimental results regardless of step size and polarizer insertion. The possible error sources are discussed in this section, including image instability caused by the uncertainty of the camera aperture, phase unwrapping error, and image noise due to the flash frequency generated between the projector and the camera.

5.1 Error due to Uncertain Camera Aperture

The CMOS camera (Blackfly S USB3 30 FPS used in this work was manually set for aperture size and focal length., Since the ISO (ISO is the camera’s sensitivity to light as it pertains to either film or a digital sensor) value could not be adjusted in the program, the camera would automatically have a smaller aperture (manual focus) may indirectly lead to an increase in the camera's ISO setting, which brings more noise to the images, which in turn affects the overall signal-to-noise ratio of the images. In addition, the different height of the printing platform and focusing area in each experiment can make it difficult to determine the aperture size corresponding to different scenes. Experiments with large apertures resulted in clear images but overall severe overexposure and increased noise. As shown in Figure 23, the number and proportion of over-

exposed points in the images differ with different exposure scenes. At the same time, due to the large aperture, the camera focus area will be limited and cannot be applied to a large area for process monitoring. As shown in Figure 29, the scan line can be clearly observed in the square in the left focus area (within the red border), but the set scan line cannot be clearly seen in the square on the right (within the green border) and is severely over-exposed.

Therefore, we need to find a suitable way to quantify the camera aperture, which can ensure a large capture area while improving the image's resolution can keep the overexposure ratio low and will not affect the collection of fringes information.

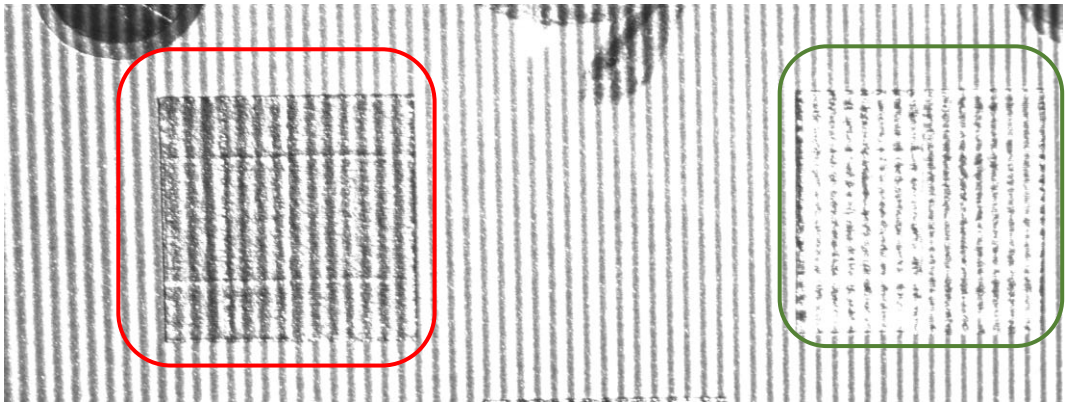

Fig. 29. Same camera captured images with different resolutions due to aperture size.

5.2 Error from Unwrapping phase process

Two types of phase unwrapping errors can occur. The first type is the error caused by noise, which is uniformly distributed and discrete. Therefore, it can be easily detected and eliminated by various elimination methods (such as the 2D FFT filtering method used in this

article). The second one is the jump error caused by two main reasons, which are not completely solved yet in this work, as shown in Figure 30.

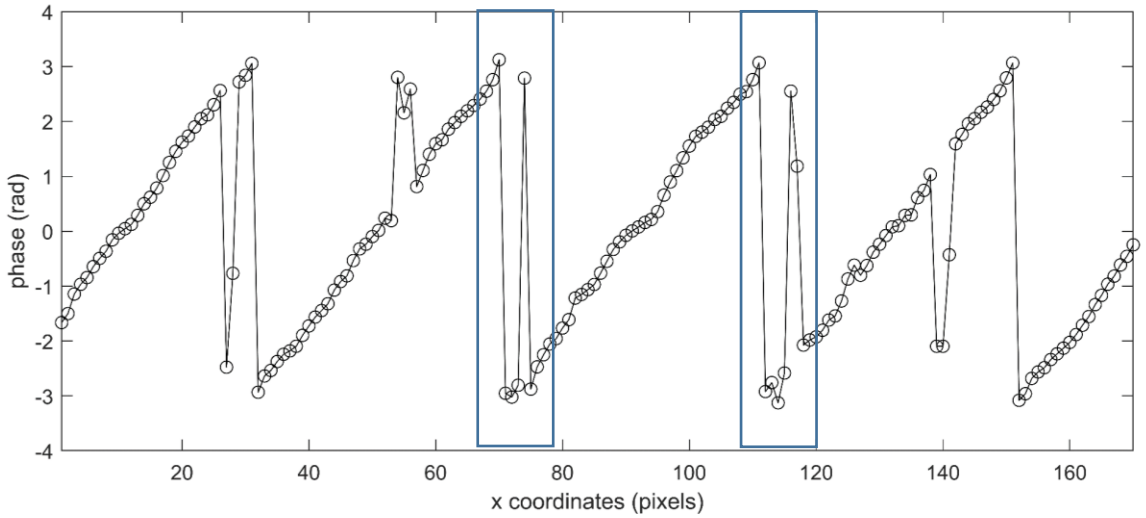

Fig. 30. Jump error caused by arctangent calculatrion in wrapped phase map.

The first reason is that the tangent calculation in phase extraction leads to unstable jumps near the discontinuity of the wrapped phase (in the blue box in Figure 30), so the jump edges of the wrapped phase are unreliable for phase unwrapping. Using common phase unwrapping methods can cause the unwrapped phase map to have large inaccuracies due to jump errors. Another reason is that the projector scatter causes misalignment between the wrapped phase and the stripe order, which leads to significant errors in phase unwrapping. The jump errors are periodically distributed in bands, so it is difficult for the post-elimination method to distinguish the jump errors from the abrupt edges of the object when the width of the error region is large. Therefore, the jump error is more difficult to be eliminated than the error caused by noise in the FPP. In the future, we will use advanced phase unwrapping methods such as the one reported in [Wu Z, Guo W, Lu L, et al. 2021].

5.3 Error from Projector-camera Flickering

In essence, the camera is not always "open". The camera opens and closes the shutter at a certain frequency in order to record images on the CMOS sensor. Because the frequency between the camera and the light source (projected from the projector) is not synchronized, camera flickering may be encountered as shown in Figure 31(a). Flickering can cause irregular fringe patterns in the images recorded by the camera, can affect the intensity calibration of the projector-camera, and can result in a serious loss of accuracy of the FPP method. As shown in Figure 32, the difference in fit between the C_{xy} calibration factor with severe flash frequency problem (R^2 = 0.741) and the C_{xy} calibration factor with reduced flash frequency (R^2 = 0.998) is large. To solve this problem, we tried to match the frame rate of the camera to the frequency of the projector. The default frame rate of the projector is 120 Hz, and we adjusted the frame rate of the camera to 30 Hz for synchronization, but the flickering cases at different exposure times remained different, as shown in Figure 31(b)(c).

After empirical debugging, we tentatively adopted 30Hz framerate and 25000μs exposure time as the camera parameters for all experiments. However, we were unable to determine whether there was still an invisible flickering under this parameter, and we will need to use other methods to address it in future experiments.

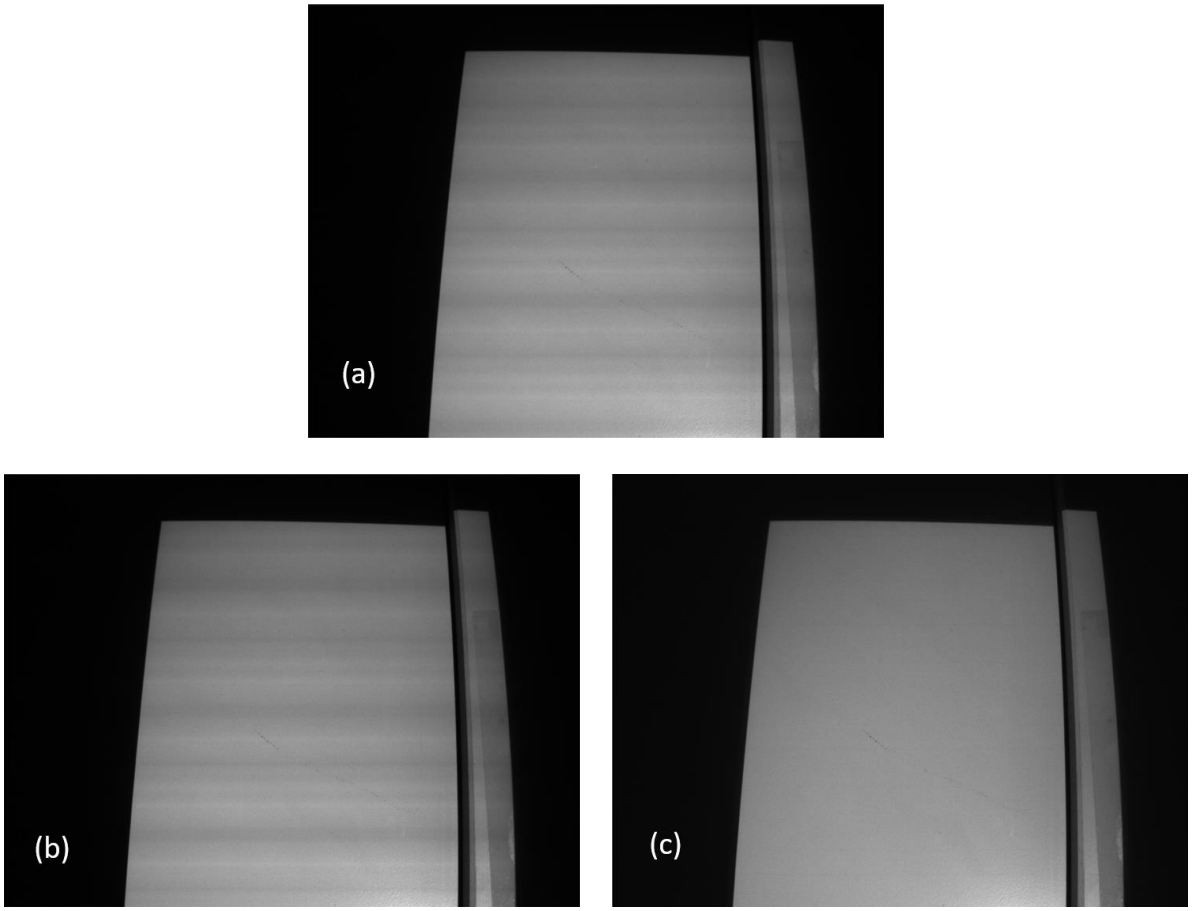

Fig. 31. Camera flickering comparison. (a) Camera default setup with 31.03 Hz and 15000 µs. (b) Camera setup with 30 Hz and 15000 µs. (c) Camera setup with 30 Hz and 25000 µs.

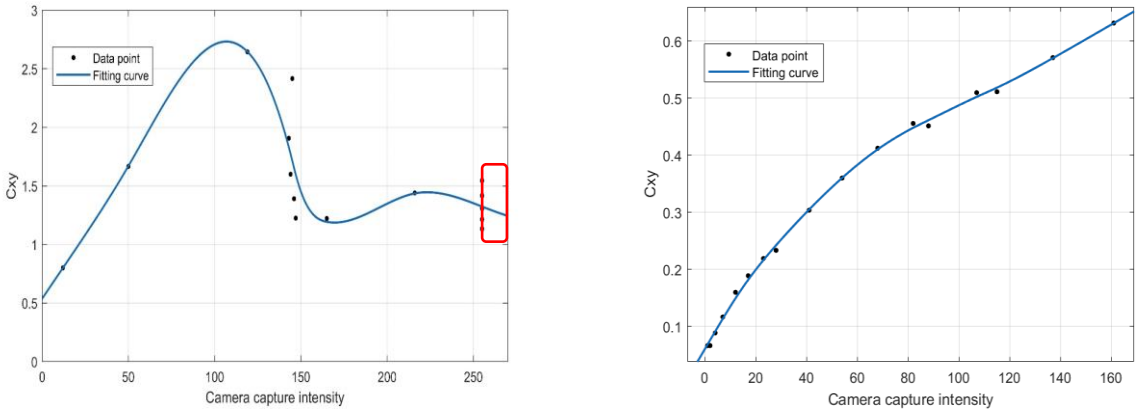

Fig. 32. Flickering (left) VS no flickering (right) C_{xy} calibration result comparison.

6.0 Conclusion and Future work

6.1 Conclusion for the Developed FPP Method

FPP is a 3D reconstruction measurement method for capturing 3D information about the powder bed and printing area of the process in metal AM. In-situ process monitoring using FPP in LPBF has been widely used, but due to the characteristics of metal materials, there are too many specular reflective areas on the metal surface during the in-situ monitoring, and the projector projects to the surface of the printed object fringe information are lost. This problem leads to a decrease in the accuracy of defect monitoring during the LPBF process and affects the efficiency of the subsequent real-time control strategy. Therefore, in this work, we added a height calibration and projector-camera intensity calibration process based on the existing conventional FPP system, and intervened a linear polarizer into the system, and tried to improve the accuracy of the FPP method with a higher step size.

In this work, we present in detail the principle of the FPP system, the mathematical and physical model of the calibration system, and two potential methods to improve the LPBF-specific FPP measurement performance using more phase steps and linear polarizers. Finally, we verify the feasibility of our modified FPP methods for surface measurement by comparing the FPP analysis results against ex-situ Keyence microscope. Also, we elaborate the corresponding error sources and improvement methods. From the experiments in this paper, we also learn that the FPP method has a certain resolution limitation in height measurement. In this work, we introduce the FPP method to improve the accuracy by increasing the number of step phases and to reduce the information loss due to overexposure of the measured surface by introducing a linear polarizer.

We can measure with high accuracy in an area of 2 mm × 2 mm, where we can achieve a minimum detection size of ~26 μm and a vertical measurement range of 100 μm (this resolution is suitable for larger defects). Linear polarizers can substantially reduce overexposure during image acquisition, but in FPP applications are only capable of 3D reproduction for larger defects or height profiles (>30 μm). For structures smaller than 30 μm, the linear polarizer smoothens the characteristic height, also as a result of its attenuated signal-to-noise ratio.

6.2 Future Work

As shown in the previous experiments, the goal of this work is to explore the feasibility and accuracy of the FPP method with and without a polarizer in 3 step phase shifting versus 12 step phas shifting. What is known is that the involvement of the polarizer does reduce the overexposure in the images captured by the camera, but it also has a negative effect on the resolution of the images and leads to the smoothing of the height curve and the inability to monitor defects and morphologies smaller than 10 μm. Therefore, in order to further evaluate the applicability of polarizers in the FPP method, we need to use the transmission angle between polarizers as one of the experimental control factors to explore the optimal high-resolution angle through more groups of controlled experiments. Second, since the experiments in this work are all static, we should focus on how to introduce the polarizers into the in-situ monitoring process, so that the dynamic LPBF system will have more factors to be considered.

Another future work is to solve the problem of camera aperture and flickering. The current camera aperture does not support us to obtain a wide range of sharp focus area (above 50mm diameter), and the images outside the sharp focus area will be affected by distortion and other

effects, making it impossible to perform FPP analysis properly, so we need more experimental pre-processing to quantify the aperture size to suit different experimental needs. For the camera flickering problem, it needs to be solved from the hardware side by considering the use of control elements to synchronize the camera shutter frequency exactly with the projector (i.e., 120 Hz corresponds to 120 FPS).

Appendix A MATLAB Code

Projector-camera Intensity Correction (smoothspline regression)

```
format long; clear; clc;
n = 17; % number of the intensity images
Cxy = cell(n,1);
I_img = cell(n,1);
mm = linspace(15,255,n);
stored = cell(170,170); % perspective image size
for m = 1:n
    myFolder = ['G:\Master thesis data\-11162022_using\cxy\wlp\1\'];
    filePattern = fullfile(myFolder, '*.Bmp');
    imgFiles = dir(filePattern);
    N = length(imgFiles);
    I = zeros(170,170);
    baseFileName = imgFiles(m).name;
    fullFileName = fullfile(myFolder, baseFileName);
    Ii = imread(fullFileName);
    Ii= im2gray(Ii);
    Ii = double(Ii);
    I_img{m,1} = Ii;
    C = Ii / mm(m);
    Cxy{m,1} = C;
end
%%
Cxy_fit_spline = cell(170,170); %set an image size cell
for j = 1:170
    for k = 1:170
        for i = 1:n
            Cxy_double = cell2mat(Cxy(i,1));
            corr_factor_r(i) = Cxy_double(j,k);
            img_intensity = cell2mat(I_img(i,1)); %actual image intensity
            coeff_img_int_r(i) = img_intensity(j,k);
            proj_inten(i) = mm(i);
        end
        [f,gof] = fit(coeff_img_int_r',corr_factor_r','smoothingspline');
        c = coeffvalues(f);
        Cxy_fit_spline(j,k) = {c};
    end
end
```

Out-of-plane Calibration

```
load ('cxy_fit_wlp.mat','Cxy_fit_spline');
n = 10;%define the number of height position.
H = 100; %define the range of height in um.
phi = cell(n,1);
uphi = cell(n,1);
for i = 1:n
```

```
    phi_i = p_shift(['G:\Master thesis data\-11162022_using\kxy\wlp
pers\',num2str(i),''],Cxy_fit_spline);
    phi{i,1} = phi_i;
end
%%
uphi_r = itoh_unwrap_c(cell2mat(phi(3,1)));
uphi_r = fitting(uphi_r);
%%
[w,h] = size(uphi_r);
parfor i = 1:n
    U = unwrap_ref(cell2mat(phi(i,1)),uphi_r);
    uphi{i,1} = U;
end
%%
delta = cell(n,1);
for i = 1:n
    del = uphi{i}-uphi_r;
    delta{i,1} = del;
end
%%
K = cell(2,1);
Kk = zeros(w,h,2);
y = zeros(n,1);
yy = cell(w,h);
x = linspace(345.00,344.91,n);
%calibration size
for i =1:170
    for j = 1:170
        for z = 1:n
            M = cell2mat(uphi(z,1));
            y(z,1) = M(i,j);
        end
        [K,gof] = polyfit(y(3:6),x(3:6),1);
        yy(i,j)={y};
        Kk(i,j,1) = K(1);
        Kk(i,j,2) = K(2);
    end
end
Kxy = abs(Kk(:,:,1));
mesh(Kxy);
caxis([0.36 0.48]);
%% the phase shift algorithm
function M = p_shift(path,f) % Apply the pixel-wise Cxy calibration
fp = fullfile(path, '*.Bmp'); % The image format is .bmp
img = dir(fp);
Y = 0;
X = 0;
n = length(img);
for k = 1:3 % step size
    fpName = img(k).name;
    imgName = fullfile(path, fpName);
    II = imread(imgName);
    if size(II,3)==3
        II = rgb2gray(II);
    end
```

```
    II=double(II);
    for i = 1:170
        for j = 1:170
            II(i,j)=ppval(f{i,j},II(i,j)).*II(i,j);
        end
    end
    sigma = 2*k*pi/n;
    Y = Y + sin(sigma) * II;
    X = X + cos(sigma) * II;
end
M = (atan2(-Y,X));
end
%%
%Unwrap the image using the Itoh algorithm: the second method is performed
%by sequentially unwrapping the all columns, one at a time.
function [Iunwrapped] = itoh_unwrap_c(Iwrapped)
[m n] = size(Iwrapped);
Iunwrapped = Iwrapped;
%%unwrapped columns
for i=1:n
 Iunwrapped(end:-1:1,i) = unwrap(Iunwrapped(end:-1:1,i));
end
% Then sequentially unwrap all the rows
for i=1:m
 Iunwrapped(i,:) = unwrap(Iunwrapped(i,:));
end
end
%% referece-guided phaes unwrapping
function phi_u=unwrap_ref(phi,phi_ref)
    phi = phi +2*pi*round((phi_ref-phi)/(2*pi));
    [w,h] = size(phi);
    phi = fitting(phi);
    dphi = zeros(w, h);
    phi2 = phi - dphi;
    dphi = F_filter(dphi);
    uphi = dphi + phi2;
    phi_u = uphi;
end
%%
function P = fitting(M)
[w,h] = size(M);
x = 1:h;
x2 = (1:w)';
parfor i = 1:w
A = polyfit(x,M(i,:),2);
y = A(1).*x.^2+A(2).*x.^1+A(3);
M(i,:) = y;
end
parfor j = 1:h
A = polyfit(x2,M(:,j),2);
y = A(1).*x2.^2+A(2).*x2.^1+A(3);
M(:,j) = y;
end
P = M;
end
```

```
%% 2D Fourier filtering
function uphi=F_filter(phi)
[w,h]=size(phi);
% define filted spatial frequency (number of fringe cycle in each direction)
fyy = 5;
fxx = 0;
% define filter radius
rx = 70;
ry = 13;
% define centern point
cY=w/2;
cX=h/2;
% fast 2D fourier transform
FT=fftshift(fft2(phi));
for k = 1:3
    fx = k*fxx; fy = k*fyy;
FT(floor(cY-ry):ceil(cY+ry),floor(cX-fx-rx):ceil(cX-fx+rx))=0;
FT(floor(cY+fy-ry):ceil(cY+fy+ry),floor(cX-rx):ceil(cX+rx))=0;
FT(floor(cY-ry):ceil(cY+ry),floor(cX+fx-rx):ceil(cX+fx+rx))=0;
FT(floor(cY+fy-ry):ceil(cY+fy+ry),floor(cX-rx):ceil(cX+rx))=0;
end
% delete high frequency noise
FT(1:ry,floor(cX-rx):ceil(cX+rx))=0;
FT(end-ry:end,floor(cX-rx):ceil(cX+rx))=0;
FT(floor(cY-ry):ceil(cY+ry), 1:rx)=0;
FT(floor(cY-ry):ceil(cY+ry), end-rx:end)=0;
% inverse fourier transform
uphi = real(ifft2(ifftshift(FT)));
end
```

Fringe Projection Profilometry Code

```
%%
clear;clc;format long;
height_c_rxy = zeros(170,170);
load ('cxy_fit_wlp.mat','Cxy_fit_spline');
load ('kxy_wtlp_1116.mat','Kxy');
%%path of target images
path = ['G:\Master thesis data\-11162022_using\3step\wlp\selected\pers']; % Fringe
projection images
path2 = ['G:\Master thesis data\-11162022_using\ref\3step\wlp']; % Reference images
phi_t = p_shift(path,Cxy_fit_spline); % need to obtain Cxy from Projector-camera
Intensity Correction
phi_r = p_shift(path2,Cxy_fit_spline);
uphi_rr = itoh_unwrap_c(phi_r);
uphi_r = fitting(uphi_rr);
uphi_t = unwrap_ref(phi_t,uphi_r);
z =F_filter(uphi_t-uphi_r);
%%
height_c_rxy = -z.*Kxy*1000; % obtain height matrix (need Kk from the vertical
calibration)
aheight=abs(height_c_rxy);
```

Bibliography

(1) Sachs, Emanuel, et al. "Production of injection molding tooling with conformal cooling channels using the three dimensional printing process." Polymer Engineering & Science 40.5 (2000): 1232-1247.

(2) Ian Gibson, Ian Gibson. "AM technologies 3D printing, rapid prototyping, and direct digital manufacturing." (2015).

(3) Mani, Mahesh, et al. "Measurement science needs for real-time control of AM powder bed fusion processes." (2015).

(4) Sola, Antonella, and Alireza Nouri. "Microstructural porosity in AM: The formation and detection of pores in metal parts fabricated by powder bed fusion." Journal of Advanced Manufacturing and Processing 1.3 (2019): e10021.

(5) Gu, Dongdong. Laser AM of high-performance materials. Springer, 2015.

(6) Aoyagi, Kenta, et al. "Simple method to construct process maps for AM using a support vector machine." AM 27 (2019): 353-362.

(7) Calignano, Flaviana, et al. "Influence of process parameters on surface roughness of aluminum parts produced by DMLS." The International Journal of Advanced Manufacturing Technology 67.9 (2013): 2743-2751.

(8) Stimpson, Curtis K., et al. "Roughness effects on flow and heat transfer for additively manufactured channels." Journal of Turbomachinery 138.5 (2016): 051008.

(9) Tian, Yang, et al. "Influences of processing parameters on surface roughness of Hastelloy X produced by selective laser melting." AM 13 (2017): 103-112.

(10)Leon, Avi, and Eli Aghion. "Effect of surface roughness on corrosion fatigue performance of AlSi10Mg alloy produced by Selective Laser Melting (SLM)." Materials Characterization 131 (2017): 188-194.

(11)Nagalingam, Arun Prasanth, and S. H. Yeo. "Surface finishing of additively manufactured Inconel 625 complex internal channels: A case study using a multi-jet hydrodynamic approach." AM 36 (2020): 101428.

(12)Campbell, Ian, David Bourell, and Ian Gibson. "AM: rapid prototyping comes of age." Rapid prototyping journal (2012).

(13)Ian Gibson, Ian Gibson. "AM technologies 3D printing, rapid prototyping, and direct digital manufacturing." (2015).

(14)Everton, Sarah K., et al. "Review of in-situ process monitoring and in-situ metrology for metal AM." Materials & Design 95 (2016): 431-445.

(15)Whitehouse, David J. "Surface metrology." Measurement science and technology 8.9 (1997): 955.

(16)Estalaki, Sina Malakpour, et al. "Predicting defects in laser powder bed fusion using in-situ thermal imaging data and machine learning." AM 58 (2022): 103008.

(17)Zhang, Haolin, et al. "A systematic study and framework of fringe projection profilometry with improved measurement performance for in-situ LPBF process monitoring." Measurement 191 (2022): 110796.

(18)Gorthi, Sai Siva, and Pramod Rastogi. "Fringe projection techniques: whither we are?." Optics and lasers in engineering 48. ARTICLE (2010): 133-140.

(19)Chen, Fang, Gordon M. Brown, and Mumin Song. "Overview of 3-D shape measurement using optical methods." Optical engineering 39.1 (2000): 10-22.

(20)Martínez, Amalia, et al. "Iterative estimation of the topography measurement by fringe-projection method with divergent illumination by considering the pitch variation along the x and z directions." Optics and lasers in engineering 48.9 (2010): 877-881.

(21)Jiang, Chao, et al. "The application of multi-frequency fringe projection profilometry on the measurement of biological tissues." Bio-medical materials and engineering 26.s1 (2015): S395-S403.

(22)Muyshondt, Pieter GG, Sam Van der Jeught, and Joris JJ Dirckx. "A calibrated 3D dual-barrel otoendoscope based on fringe-projection profilometry." Optics and Lasers in Engineering 149 (2022): 106795.

(23)Wei, Shuwen, et al. "Numerical landmark detection algorithm for fringe projection profilometry during autonomous robotic suturing." Advanced Biomedical and Clinical Diagnostic and Surgical Guidance Systems XX. SPIE, 2022.

(24)Zhang, Bin, et al. "In situ surface topography of laser powder bed fusion using fringe projection." AM 12 (2016): 100-107. Zhang B, Ziegert J, Farahi F, et al.

(25)Feng, Shijie, et al. "Calibration of fringe projection profilometry: A comparative review." Optics and Lasers in Engineering 143 (2021): 106622.

(26)Umeyama, Shinji, and Guy Godin. "Separation of diffuse and specular components of surface reflection by use of polarization and statistical analysis of images." IEEE Transactions on Pattern Analysis and Machine Intelligence 26.5 (2004): 639-647.

(27)Creath, K., and J. C. Wyant. "Moiré and fringe projection techniques." Optical shop testing 2 (1992): 653-685.

(28)Greivenkamp, John E. "Generalized data reduction for heterodyne interferometry." Optical Engineering 23.4 (1984): 350-352.

(29)Huang, Lei, Patrick SK Chua, and A. Asundi. "Least-squares calibration method for fringe projection profilometry considering camera lens distortion." Applied optics 49.9 (2010): 1539-1548.

(30)Wolberg, George. Digital image warping. Vol. 10662. Los Alamitos, CA: IEEE computer society press, 1990.

(31)Xiong, Yubo. In-situ Powder Bed Surface Topography for Laser-Based Metal AM Process Monitoring. Diss. University of Pittsburgh, 2021.

(32)Toshiba Teli Corporation. “Reflection and polarization of light in machine vision.” Reflection & polarization of light in machine vision (toshiba-teli.co.jp), 2020.Hu, Qingying, et al. "Shiny parts measurement using color separation." Two-and Three-Dimensional Methods for Inspection and Metrology III. Vol. 6000. SPIE, 2005.

(33)Feng, Shijie, et al. "General solution for high dynamic range three-dimensional shape measurement using the fringe projection technique." Optics and Lasers in Engineering 59 (2014): 56-71.

(34)Salahieh, Basel, et al. "Multi-polarization fringe projection imaging for high dynamic range objects." Optics express 22.8 (2014): 10064-10071.

(35)Wu, Zhoujie, et al. "Generalized phase unwrapping method that avoids jump errors for fringe projection profilometry." Optics Express 29.17 (2021): 27181-27192.

(36)Thorlabs, Inc. "Dichroic Film Polarizer’s Transmission and Extinction Ratio for Visible Light (400 - 700 nm)." Economy Film Polarizers, Thorlabs, 2012, Economy Film Polarizers (thorlabs.com).